



Delft University of Technology

## A unifying approach to subtidal salt intrusion modeling in tidal estuaries

Dijkstra, Yoeri M.; Schuttelaars, Henk M.

**DOI**

[10.1175/JPO-D-20-0006.1](https://doi.org/10.1175/JPO-D-20-0006.1)

**Publication date**

2021

**Document Version**

Final published version

**Published in**

Journal of Physical Oceanography

**Citation (APA)**

Dijkstra, Y. M., & Schuttelaars, H. M. (2021). A unifying approach to subtidal salt intrusion modeling in tidal estuaries. *Journal of Physical Oceanography*, 51(1), 147-167. <https://doi.org/10.1175/JPO-D-20-0006.1>

**Important note**

To cite this publication, please use the final published version (if applicable). Please check the document version above.

**Copyright**

Other than for strictly personal use, it is not permitted to download, forward or distribute the text or part of it, without the consent of the author(s) and/or copyright holder(s), unless the work is under an open content license such as Creative Commons.

**Takedown policy**

Please contact us and provide details if you believe this document breaches copyrights. We will remove access to the work immediately and investigate your claim.

# A Unifying Approach to Subtidal Salt Intrusion Modeling in Tidal Estuaries<sup>✉</sup>

YOERI M. DIJKSTRA<sup>a</sup> AND HENK M. SCHUTTELAARS<sup>a</sup>

<sup>a</sup> *Delft Institute of Applied Mathematics, Delft University of Technology, Delft, Netherlands*

(Manuscript received 16 January 2020, in final form 20 October 2020)

**ABSTRACT:** The salinity structure in estuaries is classically described in terms of the salinity structure as well mixed, partially mixed, or salt wedge. The existing knowledge about the processes that result in such salinity structures comes from highly idealized models that are restricted to either well-mixed and partially mixed cases or subtidal salt wedge estuaries. Hence, there is still little knowledge about the processes driving transitions between these different salinity structures and the estuarine parameters at which such a transition is found. As an important step toward a unified description of the dominant processes driving well-mixed, partially mixed, and salt wedge estuaries, a subtidal width-averaged model applicable to all these salinity structures is developed and systematically analyzed. Using our model, we identify four salinity regimes, resulting from different balances of dominant processes. It is shown that each regime is uniquely determined by two dimensionless parameters: an estuarine Froude and Rayleigh number, representing freshwater discharge and tidal mixing, respectively, resulting in a classification of the regimes in terms of these two parameters. Furthermore, analytical expressions to approximate the salt intrusion length in each regime are developed. These expressions are used to illustrate that the salt intrusion length in different regimes responds in a highly different manner to changes in depth and freshwater discharge. As one of the key results, we show that there are only very weak relations between the process-based regime of an estuary and the salt intrusion length and top–bottom stratification. This implies that the salinity structure of an estuary cannot be uniquely matched to a regime.

**KEYWORDS:** Estuaries; Baroclinic flows; Nonlinear dynamics; Salinity; Classification; Differential equations

## 1. Introduction

The salinity structure in estuaries is classically described as well mixed, partially mixed, or salt wedge (Pritchard 1955). These different salinity structures are driven by different dominant balances of physical processes and therefore have different dependencies on estuarine parameters such as depth and river discharge. The basis of our understanding of these dependencies comes from idealized subtidal width-averaged models under constant forcing (steady state). It is well known that these models are not necessarily representative of real estuarine dynamics, as it has been shown that tidal and lateral processes are often important to salt intrusion (see, e.g., reviews by Fischer et al. 1979; MacCready and Geyer 2010), some estuaries are strongly characterized by tidal variations (e.g., Geyer and Farmer 1989; Simpson et al. 1990; Ralston et al. 2010), and delayed response to variable forcing is known to be important (e.g., MacCready 2007; Hetland and Geyer 2004; Lerczak et al. 2009). Nevertheless, steady-state subtidal width-averaged models are still among the state-of-the-art for identifying typical relations between salt intrusion length, depth, river discharge, and tidal mixing, and these relations continue to be useful to the interpretation of observed salinity distributions (Monismith et al. 2002; Ralston et al. 2008; MacCready

and Geyer 2010; Aristizábal and Chant 2013; Chant et al. 2018). However, existing subtidal width-averaged models rely on highly restrictive assumptions that make them applicable to either well-mixed, partially mixed, or salt wedge estuaries but not to all these types of estuaries at once. As a result, there is still little knowledge of the differences in dominant processes that result in the different types of salinity structures and the parameter values for which the transition from one type of salinity structure to another occurs.

The first subtidal width-averaged model was developed by Hansen and Rattray (1965) and is applicable to well-mixed and partially mixed estuaries. By restricting their analysis to these types of estuaries, it could be assumed that the along channel salinity gradient is depth uniform and that momentum advection (or inertial) terms are negligible. These assumptions reduce the highly nonlinear differential equations for water motion and salinity to one simple equation. Hansen and Rattray (1966) show in a classification diagram that, depending on the model parameters, this equation allows two types of dominant salt transport balances: between either river-induced flushing and tidal dispersion or river-induced flushing and subtidal advective transport. The first balance is typically associated with well-mixed estuaries. The upstream transport in this balance is due to a semiempirical parameterization of tidal dispersion as a Fickian diffusion process (e.g., Bowden 1965). The latter balance, as argued by Chatwin (1976), is taken to be the most important balance in partially mixed estuaries. Chatwin (1976) furthermore showed that the subtidal advective transport is primarily related to gravitational vertical shear dispersion; the covariance between the flow velocity and the salinity induced by gravitational circulation. The model was further generalized and analyzed by MacCready (2004).

<sup>✉</sup> Supplemental information related to this paper is available at the Journals Online website: <https://doi.org/10.1175/JPO-D-20-0006.s1>.

Corresponding author: Yoei M. Dijkstra, [y.m.dijkstra@tudelft.nl](mailto:y.m.dijkstra@tudelft.nl)

He showed that the dispersive balance and Chatwin's advective balance may both occur in different parts of a single estuary. Guha and Lawrence (2013) further refined these results by showing that the dominant balance, dispersive or advective, only depends on two dimensionless parameters in the context of this model. These parameters are an internal Froude number and a tidal Froude number, representing the strength of the river discharge and tidal mixing, respectively.

A completely different type of model is used to describe strong stratification in salt wedge estuaries and fronts: the two-layer model. In this type of model, the flow is separated into two layers that only interact through parameterized friction and mixing coefficients. One of the most prominent publications on subtidal two-layer models of arrested salt wedge estuaries is by Schijf and Schönfeld (1953). They assumed a stationary salt wedge with a fixed density and spatially varying height located below a fully fresh layer. Under these assumptions, the dominant balance of salt transport processes is between interfacial friction, baroclinic pressure, and momentum advection. More recently developed two-layer models include vertical profiles of the velocity and density per layer, entrainment between the layers, and empirical parameterizations of the interfacial stress (Arita and Jirka 1987; Prandle 1985; Sorgard et al. 1990). This led to refinements of the results found by Schijf and Schönfeld (1953) but without qualitatively changing the underlying salt transport balance. The need to prescribe the density per layer and interfacial friction coefficient in two-layer models is fundamentally different from the class of models for well-mixed and partially mixed estuaries, which partly resolve the density difference and apply eddy viscosity and eddy diffusivity coefficients to model friction and entrainment. Hence, the different types of model approaches are not easily unified.

Hetland and Geyer (2004) showed that a unified description of subtidal dynamics is possible using a numerical ROMS model with uniform geometry and prescribed mixing parameters. They present both partially mixed and salt wedge estuaries by varying model parameters but did not analyze the dominant processes nor systematically analyze the entire parameter space. The most prominent unified framework at present is that by Geyer and MacCready (2014), who additionally include tides in their classification. Their work is constructed on the basis of a large base of knowledge of physical processes and semi-empirically derived dimensionless numbers, linked to observations but without one unifying mathematical model to provide a direct link between a model, dominant physical processes, and stratification. Hence, there is no single theoretical framework describing the physics in the entire spectrum from well-mixed to strongly stratified estuaries.

To unify the theory of well-mixed, partially mixed, and salt wedge estuaries in a subtidal context, we develop and analyze a subtidal width-averaged model that allows for a mechanistic description of estuaries across the spectrum. The salt transport balance is analyzed by constructing a decomposition similar to that used by MacCready (2004) and Guha and Lawrence (2013). Using this decomposition, we systematically investigate the entire estuarine parameter space for along-channel uniform channels, classify the dominant balance of physical

processes in each part of this parameter space, and relate this dominant balance to the salt intrusion length and stratification.

The model, solution technique, decomposition technique, and derivation of dimensionless parameters is presented in section 2. Results are presented in section 3. This first discusses the essential dynamics in each of the four regimes (section 3a). Next, we present results for the entire estuarine parameter space, showing which regime occurs in what part of the parameter space (section 3b). Section 3c then shows the salt intrusion length and stratification in the entire parameter space. We zoom in on these results by showing the dependency between salt intrusion length, river discharge, and depth for each of the regimes in sections 4a and 4b. In section 4c we indicate the location of several estuaries within our parameter space. The main findings are summarized in section 5

## 2. Model

### a. Model equations

A subtidal width-averaged model is developed for a straight rectangular channel with fixed width  $B$ , depth  $H$ , and length  $L$ . The model domain is Cartesian with along channel coordinate  $x$ , ranging from the mouth at  $x = 0$  to the upstream boundary at  $x = L$ , and vertical coordinate  $z$  ranging from the bed at  $z = -H$  to a fixed surface at  $z = 0$  (i.e., rigid lid). The upstream boundary  $x = L$  is required to have no influence on the salinity dynamics. Hence, we choose  $L$  such that the boundary is far upstream from the salt intrusion limit.

To model the water motion and salt dynamics, turbulent motions are parameterized by an eddy viscosity and eddy diffusivity, and density differences are only taken into account in the pressure terms (i.e., Boussinesq approximation). Furthermore, the effect of salinity  $s$  on the density  $\rho$  is assumed to be linear according to  $\rho = \rho_0(1 + \beta s)$ , where  $\rho_0$  is a reference density of  $1000 \text{ kg m}^{-3}$  and  $\beta$  is the haline contraction coefficient of  $7.6 \times 10^{-4} \text{ psu}^{-1}$ . Under these assumptions, the water motion is described by the following continuity and momentum equations:

$$u_x + w_z = 0, \quad (1)$$

$$uu_x + wu_z = -g\zeta_x + g\beta \int_z^0 s_x dz' + (A_\nu u_z)_z. \quad (2)$$

Here,  $u$  is the horizontal velocity,  $w$  is the vertical velocity,  $\zeta_x$  is the surface gradient,  $g$  is the acceleration of gravity, and  $A_\nu$  is the vertical eddy viscosity. The boundary conditions to these equations are given by

$$A_\nu u_z = 0 \quad \text{at } z = 0, \quad (3)$$

$$A_\nu u_z = s_f \mu \quad \text{at } z = -H, \quad (4)$$

$$w = 0 \quad \text{at } z = 0, \quad (5)$$

$$w = 0 \quad \text{at } z = -H, \quad (6)$$

$$B \int_{-H}^0 u dz = -Q \quad \text{at } x = L, \quad (7)$$

$$-g\zeta_x + (A_\nu u_z)_z = 0 \quad \text{at } x = L. \quad (8)$$

The first condition represents a no-stress condition at the fixed surface. The second condition is a partial slip bottom friction condition and can be regarded as a linearization of a quadratic slip law with friction coefficient  $s_f$  (see, e.g., [Zimmerman 1982](#)). The third and fourth conditions require the bed to be impermeable and the surface to be a rigid lid. The fifth condition sets the inflow at the upstream boundary equal to a prescribed river discharge. Note that the river discharge is denoted by a positive number, while the flow is in negative  $x$  direction. Hence the minus sign in Eq. (7). The final boundary condition is a reduced momentum equation for the upstream boundary and requires that the velocity profile reduces to a profile corresponding to a constant river flow.

Note that by integrating the continuity Eq. (1) over depth and applying the boundary conditions for  $w$  and the river discharge condition, it is found that the cross-sectionally integrated flow should equal  $-Q$  everywhere in the estuary.

The salinity model results from salinity conservation and reads as

$$us_x + ws_z = (K_v s_z)_z + (K_h s_x)_x, \quad (9)$$

where  $K_v$  and  $K_h$  are the vertical and horizontal eddy diffusivities. This equation satisfies boundary conditions

$$K_v s_z = 0 \quad \text{at } z = 0, \quad (10)$$

$$K_v s_z = 0 \quad \text{at } z = -H, \quad (11)$$

$$us_x + ws_z = (K_v s_z)_z \quad \text{at } x = 0, \quad z \in (-H, 0], \quad (12)$$

$$s = s_{\text{sea}} \quad \text{at } x = 0, \quad z = -H, \quad (13)$$

$$s = 0 \quad \text{at } x = L. \quad (14)$$

Here, the first two conditions represent no-flux conditions at the bed and surface. The third and fourth condition for the estuarine mouth are similar to those used by [MacCready \(2004\)](#). Equation (13) sets the salinity at the bed at the mouth of the estuary equal to the ocean salinity. Equation (12) describes that the salinity in the remainder of the water column is computed using the salinity equation without horizontal dispersion (i.e.,  $K_h = 0$ ). The final boundary condition requires that the salinity vanishes at the upstream boundary.

The eddy viscosity  $A_v$  and eddy diffusivity  $K_v$  are assumed to be uniform over the depth and constant along the length of the estuary. The eddy viscosity and eddy diffusivity are related through a Prandtl–Schmidt number  $\sigma_\rho$  as  $K_v = A_v/\sigma_\rho$ . In this study, we use a constant Prandtl–Schmidt number of  $\sigma_\rho = 2.2$  ([Ralston et al. 2008](#)). The friction coefficient  $s_f$  is also assumed constant along the length of the estuary. The friction coefficient and eddy viscosity are related as

$$A_v = 0.5s_f H, \quad (15)$$

which approximately parameterizes the relation between the eddy viscosity and bed friction in a barotropic uniform flow using a  $k$ - $\epsilon$  model ([Dijkstra et al. 2017](#)). While this relation between the eddy viscosity and bed friction may not be representative for stratified estuaries with a strong baroclinic forcing, the conclusions of this study do not essentially depend

on this choice. As a result of the above relations, the model only has one calibration parameter out of  $s_f$ ,  $A_v$ , and  $K_v$ . The horizontal eddy diffusivity  $K_h$  is assumed to be a fixed spatially uniform value.

### b. Summary of the solution procedure

The system of equations is strongly nonlinear in terms of the unknowns  $u$ ,  $w$ ,  $s$ , and  $\zeta_x$  and has to be solved numerically. As we are aiming for a high numerical accuracy and a large number of simulation, the model needs to be both accurate and fast, requiring a tailored solution procedure. To get a numerically accurate solution, we combine a spectral and second-order accurate finite volume method. Next, we use a Newton–Raphson method to solve the nonlinear system. Hence, the solution method is a *numerical root-finding procedure*, and no time stepping routine is used. This eliminates the need for spinup, thereby leading to computation times of the order of seconds per simulation. The solution method is presented in detail in the online supplemental material, and only a brief outline of the method is provided below.

First,  $w$  is written in terms of  $u$  using the continuity Eq. (1), hence reducing the unknowns to  $u$ ,  $s$ , and  $\zeta_x$ . Next, to solve for  $u$  and  $s$ , we first apply a truncated spectral method in the vertical direction. This means that the vertical structure of  $u$  and  $s$  is expressed in terms of eigenfunctions of the mixing terms  $(A_v u_z)_z$  and  $(K_v s_z)_z$  which satisfy the boundary conditions at the bed and surface. Hence, the horizontal velocity and salinity are written as

$$u = \sum_{m=0}^M \beta_m(x) (-1)^m \cos(\lambda_m z), \quad (16)$$

$$s = \sum_{m=0}^M \alpha_m(x) (-1)^m \cos(\mu_m z), \quad (17)$$

in which the weight factors  $\alpha_m(x)$  and  $\beta_m(x)$  still depend on  $x$ . The coefficients  $\mu_m$  and  $\lambda_m$  are chosen in such a way that every cosine exactly satisfies the appropriate boundary conditions at the surface and bed. We substitute the above expressions for  $u$  and  $s$  in the momentum Eq. (2), salinity Eq. (9), and cross-sectionally integrated continuity Eq. (7), and we project these equations to the above eigenfunctions. This changes the three nonlinear two-dimensional equations to a system of  $2M + 1$  nonlinear one-dimensional equations for the weight factors  $\alpha_m(x)$  and  $\beta_m(x)$  and for the surface gradient  $\zeta_x(x)$ .

This one-dimensional system of equations is solved using a finite volume method on a nonuniform grid with  $j_{\text{max}}$  grid cells (i.e.,  $j_{\text{max}} + 1$  grid points). The horizontal grid adapts to the solution with every iteration to ensure the grid resolution is highest in the area with the highest salinity gradient. Furthermore, it is ensured that the change in cell size between consecutive cells is not more than 10% to prevent large errors related to the nonuniformity (see the supplemental material for details). The equations are discretized using a second-order accurate scheme, where advective terms are treated using a central scheme or a symmetry-preserving upwind scheme ([Veldman and Lam 2008](#)). This discretization changes the equations to a system of  $(2M + 1)(j_{\text{max}} + 1)$  nonlinear algebraic equations.

Finally, this system of algebraic equations is solved using a Newton–Raphson method. The Newton–Raphson method requires an initial estimate to start the iteration procedure. It is found that, for stratified estuaries, the iteration only converges when the initial estimate is close to the final solution. To find such an initial estimate, we use a *continuation procedure*. This procedure works as follows: the first initial “estimate” is a zero velocity and salinity. This initial estimate is used together with a set of parameters for which the water column is known to be well mixed, and hence the dynamics is sufficiently linear to obtain a solution for  $u$ ,  $w$ ,  $\zeta_x$ , and  $s$  starting from this trivial initial estimate. To obtain solutions for more stratified conditions, the eddy viscosity is decreased by a small amount. Using a first-order Taylor approximation of the nonlinear equations, the solution is extrapolated to find an estimated solution for the equations with decreased eddy viscosity. This estimated solution is the initial estimate for the Newton–Raphson iteration. When this iteration has converged, the eddy viscosity is decreased by another small amount, repeating the above procedure until the intended eddy viscosity is attained.

### c. Decomposition technique

As the goal of this study is to identify the dominant processes for salt intrusion, we make a decomposition of the results. Two types of decomposition technique exist. The first is based on correlations between depth-averaged and depth-varying velocity and salinity (Fischer 1972) and is often used to analyze observations or model results (e.g., Lerczak et al. 2006; Aristizábal and Chant 2013). The second type is based on assigning contributions to the velocity and salinity to particular terms in the underlying equations and is often used to analyze idealized models (e.g., MacCready 2004; Wei et al. 2016). We will use the second approach as this more directly identifies the dominant physical processes than the first approach. However, as the equations are nonlinear, this approach is not unique: as all terms in the equations interact, one needs to choose how to ascribe part of the velocity and salinity to each term. Here, we follow a method that was successfully used to analyze well-mixed to partially mixed estuaries (Hansen and Rattray 1965; Chatwin 1976; MacCready 2004; MacCready and Geyer 2010). Using this method, the horizontal velocity  $u$  and water level gradient  $\zeta_x$  are decomposed into three contributions: a river-induced barotropic part  $u_{\text{riv}}$ ,  $\zeta_{x,\text{riv}}$ , a gravitational circulation  $u_{\text{gc}}$ ,  $\zeta_{x,\text{gc}}$ , and a momentum advection-induced part  $u_{\text{adv}}$ ,  $\zeta_{x,\text{adv}}$ . These contributions follow from solving reduced forms of the momentum and depth-averaged continuity Eqs. (2) and (7), satisfying continuity (1) and boundary conditions (3)–(8). Similarly, these three contributions are computed for the vertical velocity  $w$  using the continuity Eq. (1). For the river-induced contribution, the flow is only driven by the river discharge;

$$g\zeta_{\text{riv},x} - (A_\nu u_{\text{riv},z})_z = 0, \quad (18)$$

$$B \int_{-H}^0 u_{\text{riv}} dz = -Q \forall x. \quad (19)$$

To obtain the flow due to gravitational circulation, only the baroclinic pressure is used as forcing term and the cross-sectionally integrated flow is required to vanish;

$$g\zeta_{\text{gc},x} - (A_\nu u_{\text{gc},z})_z = g\beta \int_z^0 s_x dz', \quad (20)$$

$$B \int_{-H}^0 u_{\text{gc}} dz = 0 \forall x; \quad (21)$$

The flow due to momentum advection is obtained by using the advection terms as forcing and again the cross-sectionally integrated flow is zero;

$$g\zeta_{\text{adv},x} - (A_\nu u_{\text{adv},z})_z = -(uu_x + ww_z), \quad (22)$$

$$B \int_{-H}^0 u_{\text{adv}} dz = 0 \forall x. \quad (23)$$

The terms on the right-hand side of the equations for gravitational circulation and advection are computed using the solution of the full system of equations, so that these decompositions are computed as a postprocessing step. When adding together the decomposed velocity contributions, the solution  $u$  of the fully nonlinear momentum and depth-averaged continuity equations is recovered.

The salinity is first decomposed into a depth-mean  $\bar{s}$  and a depth varying, or shear, contribution  $s'$ , such that the depth-mean of  $s'$  equals zero. Next, the shear contribution is decomposed into four contributions: a river-induced shear  $s'_{\text{riv}}$ , a gravitational shear  $s'_{\text{gc}}$ , a momentum advection-induced shear  $s'_{\text{adv}}$ , and a dispersion-induced shear  $s'_{K_h}$ . The shear contributions follow from reduced forms of the salinity Eq. (9), satisfying boundary conditions (10)–(12) and (14). To derive the river-induced, gravitational, and momentum advection-induced shear, the reduced salinity equation consists of the vertical mixing term forced by the appropriate advective contributions:

$$-(K_\nu s'_{\text{riv},z})_z = -(u_{\text{riv}} s_x + w_{\text{riv}} s_z), \quad (24)$$

$$-(K_\nu s'_{\text{gc},z})_z = -(u_{\text{gc}} s_x + w_{\text{gc}} s_z), \quad (25)$$

$$-(K_\nu s'_{\text{adv},z})_z = -(u_{\text{adv}} s_x + w_{\text{adv}} s_z). \quad (26)$$

The dispersion-induced shear follows from the vertical mixing term balanced by the dispersive term:

$$-(K_\nu s'_{K_h,z})_z = \frac{1}{B} (BK_h s_x)_x. \quad (27)$$

The above equations all satisfy the no-flux condition at the surface and bed, and, in solving, the constant of integration is chosen such that the depth average of a contribution to  $s'$  equals zero. Similar to the velocity decomposition, the right-hand sides of the above equations are computed using the solution to the fully nonlinear model, and the sum of the salinity shear contributions and the depth-mean salinity equals the solution  $s$  of the fully nonlinear salinity equation.

Finally, a decomposition is made of the cross-sectionally averaged salt transport  $T$  (in  $\text{psu m s}^{-1}$ ), which reads as

$$T = \frac{1}{H} \int_{-H}^0 (us - K_h s_x) dz = 0. \quad (28)$$

The net salt transport equals zero, since it is assumed that the river discharge has zero salinity. Substituting the decompositions

for  $u$  and  $s$  in Eq. (28), the salt transport is decomposed into the following 11 contributions:

$$T = \frac{1}{H} \int_{-H}^0 \left( \underbrace{u_{\text{riv}} \bar{s}}_{T_{\text{flushing}}} + \underbrace{u_{\text{riv}} s'_{\text{riv}}}_{T_{\text{riv-riv}}} + \underbrace{u_{\text{gc}} s'_{\text{riv}} + u_{\text{riv}} s'}_{T_{\text{gc-riv}}} + \underbrace{u_{\text{gc}} s'_{\text{gc}}}_{T_{\text{gc-gc}}} \right. \\ \left. + \underbrace{u_{\text{adv}} s'_{\text{riv}} + u_{\text{riv}} s'_{\text{adv}}}_{T_{\text{adv-riv}}} + \underbrace{u_{\text{adv}} s'_{\text{gc}} + u_{\text{gc}} s'_{\text{adv}}}_{T_{\text{adv-gc}}} + \underbrace{u_{\text{adv}} s'_{\text{adv}}}_{T_{\text{adv-adv}}} \right) \\ \left. + \underbrace{u_{\text{riv}} s'_{K_h}}_{T_{K_h\text{-riv}}} + \underbrace{u_{\text{gc}} s'_{K_h}}_{T_{K_h\text{-gc}}} + \underbrace{u_{\text{adv}} s'_{K_h}}_{T_{K_h\text{-adv}}} - \underbrace{K_h \bar{s}_x}_{T_{\text{dispersion}}} \right) dz = 0. \quad (29)$$

Two of the contributions scale with the depth-mean salinity: the transport due to river-induced flushing  $T_{\text{flushing}}$ , and the dispersive transport  $T_{\text{dispersion}}$ . The nine other terms are shear dispersion terms due to the vertical covariance of velocity and salinity shear. While this expression may only seem to complicate matters rather than elucidate them, in the next section we will show that the magnitude of many of these terms may be estimated and it will be shown in section 3 that the salt transport is dominated by only a few of these processes depending on the model parameters. Combined this means that we can do detailed analyses of reduced forms of (29) in most of the parameter space, thus identifying the dominant physical processes.

d. Typical scales

To provide further insight into the dominant contributions to the transport balance Eq. (29), we analyze the order of magnitude of the various transport terms. This is done by deriving the typical scale of each contribution to  $u$  and  $s'$  from Eqs. (18)–(27) and then computing the transport contributions in Eq. (29) using these expressions. The derivation of the typical scales is presented in appendix A, and the results are listed below:

$$T_{\text{flushing}} \sim \frac{Q}{BH} \bar{s}, \quad (30a)$$

$$T_{\text{dispersion}} \sim K_h \bar{s}_x, \quad (30b)$$

$$T_{\text{riv-riv}} \sim 3 \times 10^{-2} \left( \frac{Q}{BH} \right)^2 \frac{H^2}{K_v} \bar{s}_x, \quad (30c)$$

$$T_{\text{gc-riv}} \sim 8 \times 10^{-4} \frac{g\beta H^5}{A_v K_v} \frac{Q}{BH} \bar{s}_x^2, \quad (30d)$$

$$T_{\text{gc-gc}} \sim 5 \times 10^{-5} \frac{g^2 \beta^2 H^8}{A_v^2 K_v} \bar{s}_x^3, \quad (30e)$$

$$T_{\text{adv-riv}} \sim (10^{-7} - 10^{-4}) \frac{g^2 \beta^2 H^{10}}{A_v^3 K_v} \frac{Q}{BH} \bar{s}_x^3 \bar{s}_{xx}, \quad (30f)$$

$$T_{\text{adv-gc}} \sim (10^{-8} - 10^{-5}) \frac{g^3 \beta^3 H^{13}}{A_v^4 K_v} \bar{s}_x^4 \bar{s}_{xx}, \quad (30g)$$

$$T_{\text{adv-adv}} \sim (10^{-12} - 10^{-6}) \frac{g^4 \beta^4 H^{18}}{A_v^6 K_v} \bar{s}_x^5 \bar{s}_{xx}^2. \quad (30h)$$

We have omitted terms that scale with  $s'_{K_h}$  as they turn out to be negligibly small (see also Chatwin 1976). For the river, gravitational circulation, and dispersion contributions [Eqs. (30a)–(30e)], the presented scales are almost the same as those found by MacCready (2004). The only small difference is in the constants of proportionality and results from the fact that we use a partial slip bottom friction instead of a no-slip condition. The contributions involving momentum advection are strongly nonlinear within our decomposition method and hence no unambiguous estimate of the typical scales of these terms can be given. Our scales are derived by assuming that the right-hand sides of Eq. (22) are dominated by the flow due to gravitational circulation, which is thought to be reasonable in partially mixed estuaries (MacCready and Geyer 2010). When the advective velocity itself becomes of a similar magnitude as the flow due to gravitational circulation, this assumption is not accurate, hence explaining the large range of the coefficients in the advective transport terms. Thus, these scales mainly provide a meaningful indication of the importance of the advective terms when these advective terms are not dominant.

e. Dimensionless parameters

Following the method of Guha and Lawrence (2013), the expressions for the scale of the transport contributions may be reordered, to reveal that they only depend on two dimensionless parameters, a dimensionless salinity, and a dimensionless salinity gradient. The two parameters are

$$F_r = \frac{Q}{BHC} \text{(estuarine Froude number)}, \quad (31a)$$

$$\text{Ra} = \frac{H^2 c^2}{A_v K_h} \text{(estuarine Rayleigh number)}. \quad (31b)$$

Here,  $c$  is twice the celerity of the fastest internal wave  $c = \sqrt{g\beta s_{\text{sea}} H}$  (e.g., MacCready and Geyer 2010). The dimensionless salinity is a function of  $x$  and is defined as

$$\Sigma(x) = \frac{\bar{s}(x)}{s_{\text{sea}}}. \quad (32)$$

To define the dimensionless salinity gradient, the along-channel coordinate is scaled as

$$x^* = x \frac{c}{K_h}, \quad (33)$$

so that the dimensionless salinity gradient is given by  $\Sigma_{x^*}(x)$ .

Our definitions of the estuarine Froude number  $F_r$  and dimensionless salinity  $\Sigma$  are consistent with those by Guha and Lawrence (2013). The estuarine Rayleigh number was introduced by Hansen and Rattray (1965) as a general measure for (the inverse of) mixing. Alternative measures for mixing have been used by other authors in their classification schemes. For example, the tidal Froude number  $F_T$  of Guha and Lawrence (2013) measures mixing and is related as  $\text{Ra} = \tilde{F}_T^{-2}$  with the addition of specific parameterizations for  $A_v$  and  $K_h$  in terms of the tidal velocity. Similarly, the mixing parameter  $M$  used by Geyer and MacCready (2014) combines a tidal Froude number with the Stokes number and semiempirical parameterizations

TABLE 1. Default parameter values.

| Parameter        |                                                                   | Value                                 |
|------------------|-------------------------------------------------------------------|---------------------------------------|
| $B$              | Width                                                             | 1 km                                  |
| $H$              | Depth                                                             | 20 m                                  |
| $K_h$            | Horizontal dispersion coefficient                                 | $250 \text{ m}^2 \text{ s}^{-1}$      |
| $s_{\text{sea}}$ | Ocean salinity                                                    | 30 psu                                |
| $Q$              | River discharge                                                   | $1000 \text{ m}^3 \text{ s}^{-1}$     |
| $\sigma_\rho$    | Prandtl–Schmidt number                                            | 2.2 (Ralston et al. 2008)             |
| $\beta$          | Haline contraction coefficient                                    | $7.6 \times 10^{-4} \text{ psu}^{-1}$ |
| $g$              | Acceleration of gravity                                           | $9.81 \text{ m s}^{-2}$               |
| $M$              | Number of spectral components of $u$ and $s$ [Eqs. (16) and (17)] | 20                                    |
| $j_{\text{max}}$ | Number of grid points                                             | 500                                   |
| $\Delta x$       | Grid size (adaptive to solution)                                  | 50 m–10 km                            |

of  $A_\nu$  and  $K_h$  in terms of the tidal velocity and stratification. Here we prefer the Rayleigh number in order to be exact and general without explicit parameterizations for  $A_\nu$  and  $K_h$ . Our parameter  $x^*$  is a slight modification to the length scale of Guha and Lawrence (2013), who assumed a length scale typical for estuaries dominated by gravitational circulation. The model finally includes a fifth dimensionless number: the Prandtl–Schmidt number  $\sigma_\rho$ , which we assume to be constant and do not consider in further detail.

Of these dimensionless quantities, the estuarine Froude and Rayleigh number are known parameters, as they depend fully on the prescribed model input. The dimensionless salinity and salinity gradient depend on the model output. This analysis suggests that the model describes a function  $\Sigma(x^*)$  in terms of only two input parameters  $F_r$  and  $\text{Ra}$ . In other words, the model output is fully determined by  $F_r$  and  $\text{Ra}$ .

In the remainder of this study we will additionally derive expressions for the salt intrusion length  $L_s$ , which we define as the distance from the mouth to the point where the bottom salinity equals 1 psu. A general dimensionless form of the salt intrusion length  $\mathcal{L}_s$  may be obtained by using the same scaling as the along-channel coordinate, i.e.,

$$\mathcal{L}_s = L_s \frac{c}{K_h} \text{ (dimensionless salt intrusion length)}. \quad (34)$$

### 3. Results

Default values of the parameters used in the model experiments are listed in Table 1, together with the numerical settings. To identify the possible dominant salt transport balances that may occur in the model, a sensitivity study has been conducted for a large range of values for  $F_r$  and  $\text{Ra}$  [see Eqs. (31a) and (31b)]. These ranges of  $\text{Ra}$  and  $F_r$  are obtained by varying the river discharge  $Q$  and eddy viscosity  $A_\nu$ . By analyzing the physical processes underlying the salt balance (29) for the various model configurations, four regimes have been identified. Each regime is characterized by a different balance of physical mechanisms. We will first discuss these four regimes using four typical examples (section 3a). The four regimes are then discussed for the entire parameter space spanned by  $F_r$  and  $\text{Ra}$  in section 3b. Section 3c shows

how the dimensionless salt intrusion length  $\mathcal{L}_s$  and top–bottom salinity difference depend on  $F_r$  and  $\text{Ra}$  and how this relates to the four regimes.

#### a. Four regimes

##### 1) REGIME 1: DISPERSIVE REGIME

The salt balance in the dispersive regime is dominated by a balance between river-induced flushing and dispersive processes importing salt. Hence, the salt balance (29) can be approximated by

$$B \int_{-H}^0 \left( \underbrace{-\frac{Q}{BH} \bar{s}}_{T_{\text{flushing}}} - \underbrace{K_h \bar{s}_x}_{T_{\text{dispersion}}} \right) dz = 0. \quad (35)$$

Since we assumed constant  $B$ ,  $H$ , and  $K_h$  this equation results in the well-known exponentially decaying salinity profile (Chatwin, 1976):  $\bar{s} = s_{\text{sea}} \exp[-Qx/(BHK_h)]$ . The salt intrusion length, defined here as the location where the near-bed salinity is 1 psu, may be estimated from this expression. Assuming negligible stratification and  $s_{\text{sea}} = 30$  psu, the salt intrusion length  $L_s$  reads as

$$L_s \approx \ln\left(\frac{1}{30}\right) \frac{BHK_h}{Q}. \quad (36)$$

The above expression is only approximately true, as stratification or other small salt transport contributions may modify the salt intrusion length.

A typical example of a dispersive estuary is found by choosing  $Q = 100 \text{ m}^3 \text{ s}^{-1}$ ,  $A_\nu = 0.1 \text{ m}^2 \text{ s}^{-1}$  ( $F_r = 0.0024$ ,  $\text{Ra} = 73$ ) together with the default parameter values (Table 1). Derived from the fully nonlinear model, the resulting salinity profile near the bed, near the surface, and depth-averaged is shown in Fig. 1a and the along-channel-vertical salinity profile is shown in Fig. 1b. The salinity profile is exponentially decreasing and the vertical salinity difference is essentially zero. It will be shown in section 3c, however, that the salinity distribution may show significant stratification in this regime as well. Figure 1c shows the six most important salt transport contributions from Eq. (29). As the salt transport scales with

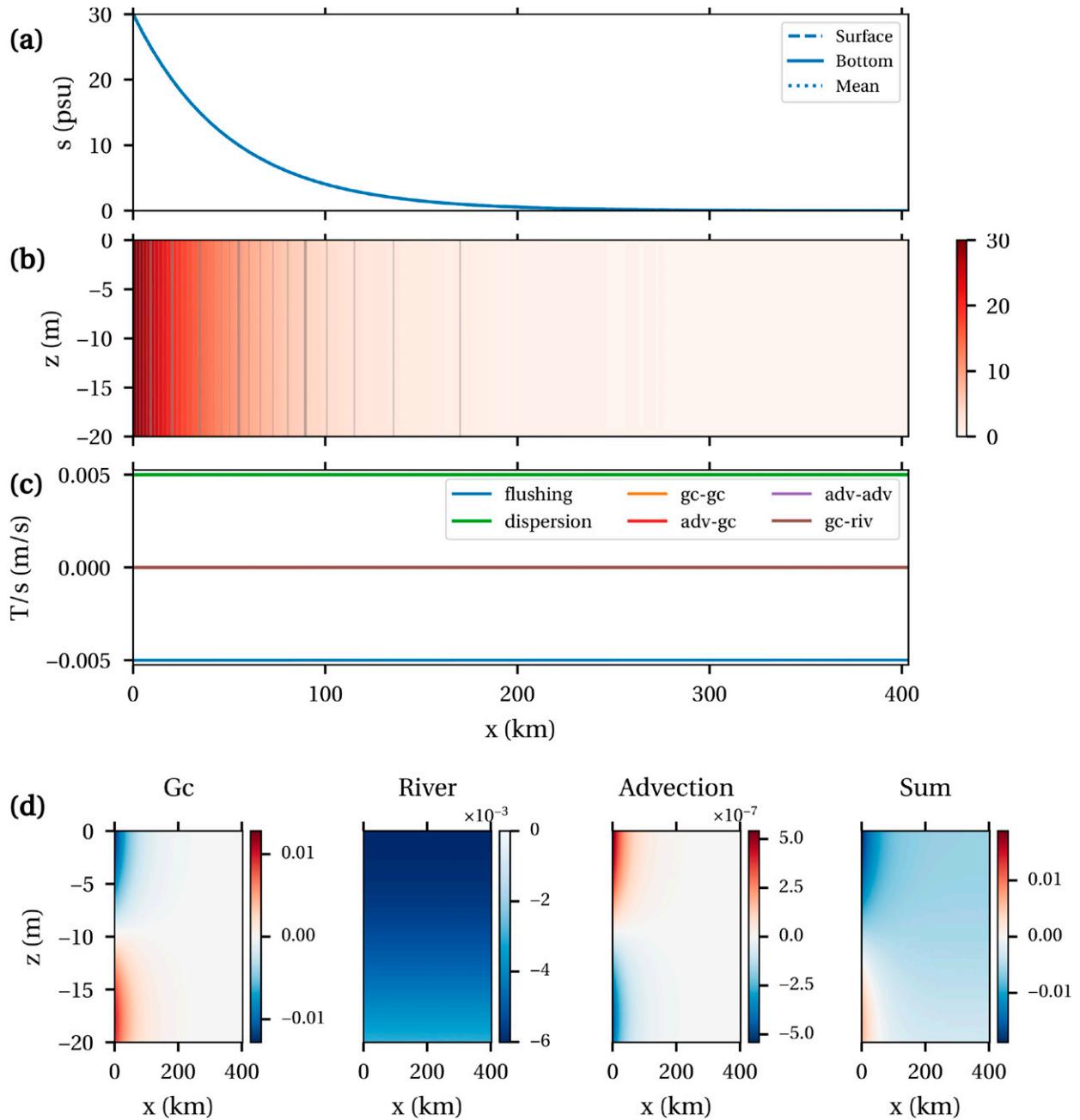


FIG. 1. Summary of the results for a case illustrating regime 1 using  $F_r = 0.0024$ ,  $Ra = 73$ . (a) The along-channel salinity profile. Note that the different lines are plotted on top of each other. (b) Salinity in the  $x$ - $z$  plane. The gray lines indicate the salinity contours with contours each 1 psu between 1 and 30 psu and thick contours at 5, 10, 15, 20, 25, and 30 psu. (c) Contributions to the cross-sectionally averaged transport divided by the depth averaged salinity (positive: importing, negative: exporting). (d) Contributions to the horizontal velocity plotted in the  $(x, z)$  plane and the total horizontal velocity (shown in the right panel).

the salinity, it vanishes near the limit of the salt intrusion. To nonetheless visualize the transport contributions in the entire estuary including near the salt intrusion limit, Fig. 1c shows the transport normalized by the local depth-averaged salinity. The figure shows that flushing and dispersion are clearly the dominant transport processes and that Eq. (35) describes the dominant balance.

The decomposition of the horizontal velocity field is shown in Fig. 1d. The main flow components are the gravitational circulation and river flow. Momentum advection is many orders of magnitude smaller. The gravitational circulation in this case is sufficiently strong compared to the river flow to result in a flow directed upstream near the bottom of the water column in the area of salinity intrusion. This is not necessarily the

case in all estuaries in this regime: a unidirectional subtidal flow in downstream direction in the entire estuary may also be observed, as shown by Hansen and Rattray (1966).

## 2) REGIME 2: CHATWIN'S REGIME

Chatwin (1976) describes a subtidal salt balance between river-induced flushing and import due to the interaction between river gravitational circulation ( $u_{gc}$ ) and the sheared salinity field caused by gravitational circulation ( $s'_{gc}$ ). The approximate salt balance in the Chatwin regime reads as

$$B \int_{-H}^0 \underbrace{-\frac{Q}{BH} \bar{s}}_{T_{\text{flushing}}} + \underbrace{u_{gc} s'_{gc}}_{T_{gc-gc}} dz = 0. \quad (37)$$

Chatwin (1976) provides an approximate solution to this equation by assuming that  $s_x$  is uniform over the entire water column and can be represented by  $\bar{s}_x$ . This assumption means that explicit analytical expressions can be obtained for  $u_{gc}$  and  $s'_{gc}$  (see, e.g., MacCready 2004). Using these expressions together with Eq. (37), the resulting along-channel depth-mean salinity profile is given by

$$\bar{s} = \bar{s}_{(x=0)} \left( \frac{x_L - \frac{2}{3}x}{x_L} \right)^{3/2} \quad (x \leq x_c). \quad (38)$$

Here,  $\bar{s}_{(x=0)}$  is the depth-averaged salinity at the mouth, which may be smaller than  $s_{sea}$  if there is stratification at the mouth. The parameter  $x_L$  is a measure for the length of the salt intrusion (but not the same as the salt intrusion length) and equals  $x_L = 0.036[(g^2 \beta^2 \bar{s}_{(x=0)}^2 H^9 / A_\nu^2 K_\nu)(B/Q)]^{1/3}$ . Note this expression has a slightly different coefficient to MacCready (2004) as we have different bottom boundary condition. The corresponding salt intrusion length may be obtained by again assuming negligible stratification, so that Eq. (38) holds for the bottom salinity. Solving the equation for the location where the bottom salinity equals 1 psu, and using  $s_{sea} = 30$  psu, the resulting salt intrusion length is then given by

$$L_s \sim 0.05 \sigma_\rho^{1/3} \frac{g^{2/3} \beta^{2/3} B^{1/3} H^3}{Q^{1/3} A_\nu} \bar{s}_{(x=0)}^{-2/3}. \quad (39)$$

If the stratification at the mouth were negligible, the salt intrusion length given here scales identically as the length scale  $L_{E3}$  used by MacCready (2004), with a small difference in the value of the coefficient because we use a partial slip bottom friction instead of no-slip.

A typical example of the Chatwin regime is found by setting  $Q = 1000 \text{ m}^3 \text{ s}^{-1}$  and  $A_\nu = 1.10^{-3} \text{ m}^2 \text{ s}^{-1}$  ( $F_r = 0.024$ ,  $Ra = 7300$ ). Figures 2a and 2b show the salinity distribution, with a top–bottom stratification of over 10 psu at the mouth. The blue solid and dashed lines in Fig. 2a, representing the surface and bottom salinity, show that this stratification results in a clearly different along-channel salinity gradient at the surface and the bottom. Nevertheless, the comparison between the modeled depth-mean salinity profile (blue dotted line) and Chatwin's depth-mean salinity profile (black dotted line) is very good. Clearly, the relatively large  $s_x$  at the bottom is balanced by the relatively small  $s_x$  at the surface so that Chatwin's solution is

valid. The solutions only deviate somewhat in the landward half of the salinity intrusion, where our model shows a slightly enhanced salt intrusion compared to the Chatwin solution.

Figure 2c shows the six most important salt transport contributions normalized by  $\bar{s}$ , confirming that the main balance is between the gravitational forces and river-induced flushing in most of the estuary. However, near the salt intrusion limit, the dispersive contribution dominates the gravitational contribution. It is important to stress that this is only visible because we plot the salt transport normalized by  $\bar{s}$ . In the area where the dispersive contribution is dominant, the salinity  $\bar{s}$  is smaller than 0.1 psu and all contributions to the salt transport tend to zero.

The dominance of the dispersive transport near the salt intrusion limit is a typical feature of the Chatwin regime, and it is important to understand this in detail before introducing the next regime. Looking closely at the Chatwin solution (38) for  $x \rightarrow (3/2)x_L$ , reveals that the second derivative,  $\bar{s}_{xx}$ , of this solution grows to infinity. Hence, the Chatwin balance cannot be valid as  $x$  approaches  $(3/2)x_L$  (i.e.,  $\bar{s}$  approaches 0), and other processes are required to restore the transport balance. To investigate which processes restore this balance, we substitute  $\bar{s}$  and  $\bar{s}_x$  from the Chatwin solution into the expressions for the transport contributions of Eq. (30). We investigate the relative importance of each term with respect to the river flushing term. Restricting our attention to the dominant transport contributions shown in Fig. 2c, these transport ratios scale as

$$\frac{T_{gc-gc}}{T_{\text{flushing}}} \sim \text{constant},$$

$$\frac{T_{\text{dispersion}}}{T_{\text{flushing}}} \sim \sigma_\rho^{-1/3} F_r^{-4/3} Ra^{-1} \Sigma^{-2/3},$$

$$\frac{T_{gc-riv}}{T_{\text{flushing}}} \sim \sigma_\rho^{1/3} F_r^{2/3} \Sigma^{-1/3},$$

$$\frac{T_{adv-gc}}{T_{\text{flushing}}} \sim \sigma_\rho^{-2/3} F_r^{2/3} \Sigma^{-1/3},$$

$$\frac{T_{adv-adv}}{T_{\text{flushing}}} \sim \sigma_\rho^{-4/3} F_r^{4/3} \Sigma^{-2/3}.$$

When the salinity tends to zero (i.e.,  $\Sigma \rightarrow 0$ ), the gravitational transport  $T_{gc-gc}$  remains constant relative to the river flushing, whereas the other terms tend to infinity relative to the river flushing. Hence, there must be a location where one of the terms  $T_{\text{dispersion}}$ ,  $T_{gc-riv}$ ,  $T_{adv-gc}$ , and  $T_{adv-adv}$  dominates over  $T_{gc-gc}$ . Which of these four terms dominates depends on the values of the proportionality constant,  $F_r$ , and  $Ra$ . Our solution shows that the dispersive contribution becomes the dominant term in the relevant part of the parameter space. The dispersive transport pushes the salt farther upstream near the limit of the salt intrusion compared to the Chatwin solution, explaining the somewhat larger salt intrusion in our model results than predicted by Eq. (39).

Inspection of the horizontal velocity components (Fig. 2d) shows that the velocity associated with gravitational circulation is the most important flow contribution, significantly larger than the typical river-induced flow. The resulting total subtidal flow therefore clearly shows the pattern of the estuarine

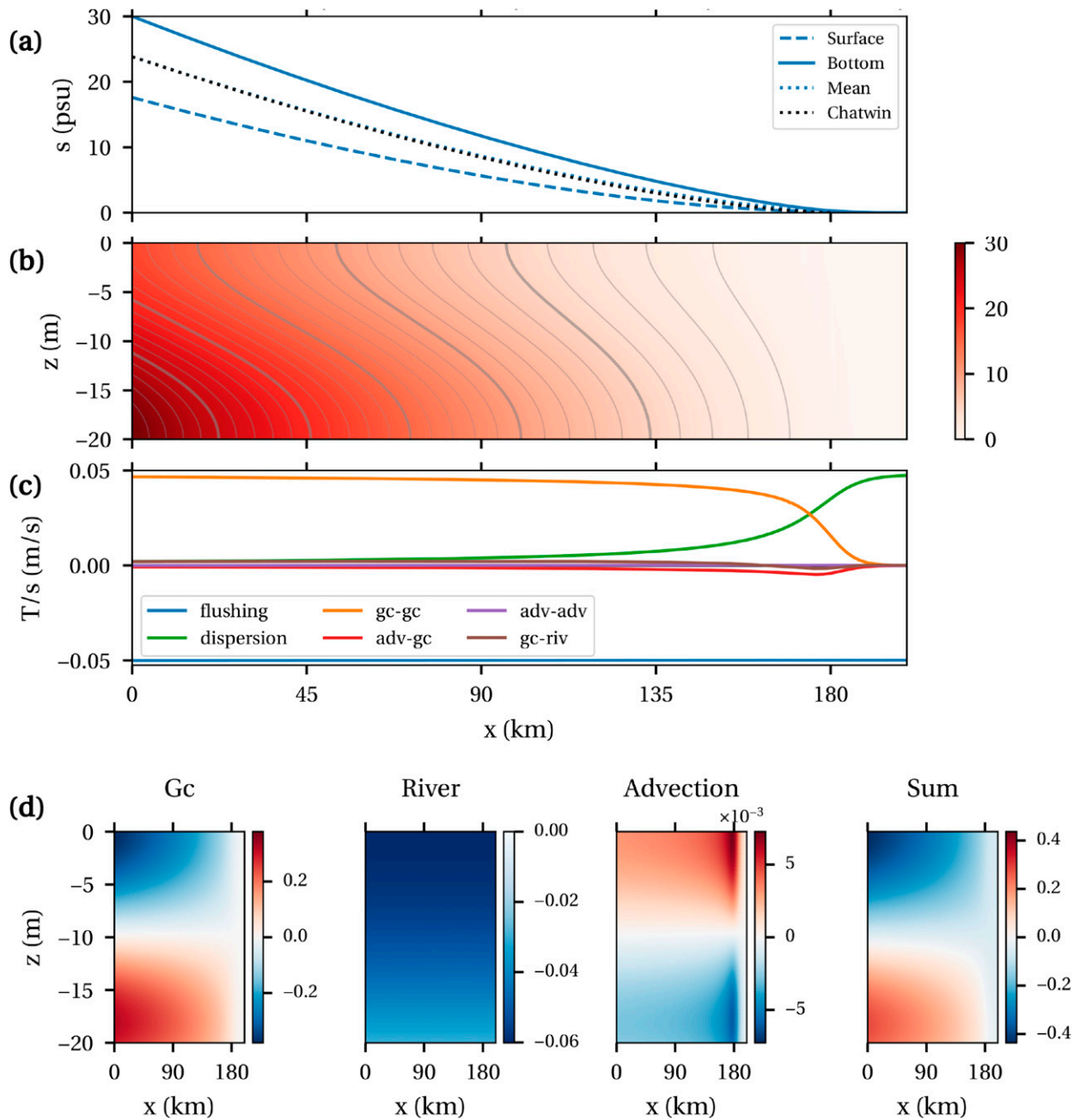


FIG. 2. As in Fig. 1, but for a case illustrating regime 2 using  $F_r = 0.024$ ,  $Ra = 7300$ .

circulation. Flow induced by momentum advection is again much smaller than the other contributions and may be ignored. Therefore, in this regime, the exchange flow as a whole scales in a similar way as the gravitational circulation as given by (Hansen and Rattray 1965).

3) REGIME 3: CHATWIN'S REGIME WITH ADVECTION DOMINATED FRONT

As in regime 2, regime 3 follows Chatwin's balance between  $T_{flushing}$  and  $T_{gc-gc}$  in most of the estuary. Therefore, Eq. (37) is

the approximate balance and Chatwin's solution [Eq. (38)] an approximate solution for this regime. The difference between regime 2 and 3 is in the balance of processes at the salt intrusion limit. While it was shown that dispersive transport is the mechanism to balance flushing at the limit of the salt intrusion in regime 2, we will show below that  $T_{adv-gc}$  may alternatively become the dominant mechanism to balance flushing at the limit of the salt intrusion. A typical example is found for  $Q = 4000 \text{ m}^3 \text{ s}^{-1}$  and  $A_r = 5 \times 10^{-4} \text{ m}^2 \text{ s}^{-1}$  ( $F_r = 0.095$ ,  $Ra = 14000$ ). Throughout the estuary, the stratification is quite

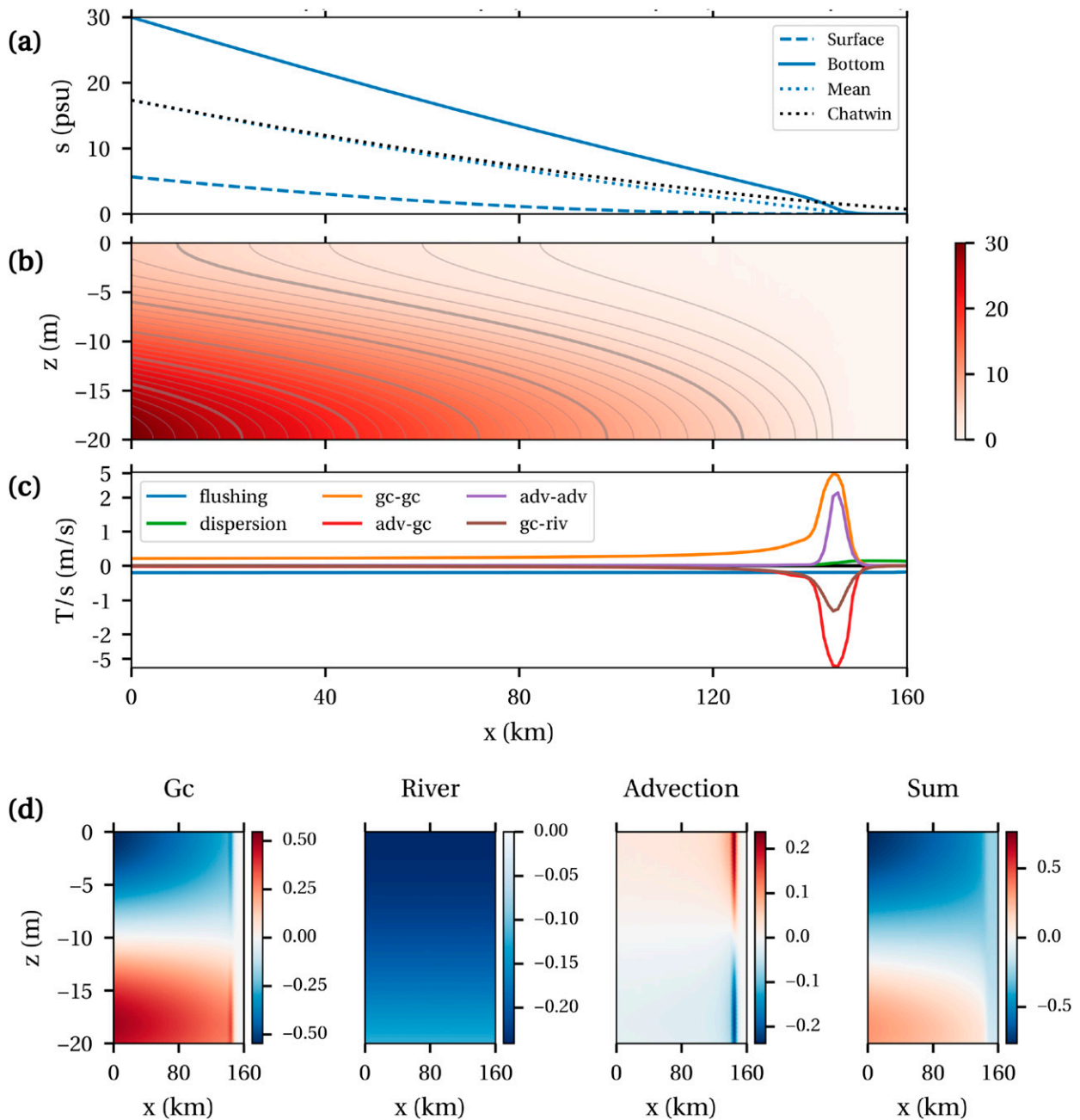


FIG. 3. As in Fig. 1, but for a case illustrating regime 3 using  $F_r = 0.095$ ,  $Ra = 14000$ .

strong, with a maximum of 24 psu at the mouth in this case (Fig. 3a). Regardless of this strong stratification and the different profiles of  $s_x$  at the surface and bottom, the comparison between the depth-mean salinity profile obtained from the model (blue dotted line) and Chatwin's solution (black dotted line) is still quite good in most of the estuary. However, the salinity goes to zero faster than the Chatwin solution near the landward limit of the salt intrusion, resulting in the formation of a weak front, with a notable increase of the along-channel salinity gradient over a short length scale. This is a characteristic difference between this regime and regime 2, where we

found enhanced salt intrusion compared to the Chatwin solution.

To explain this difference between regime 2 and 3, we look at the most important transport processes normalized by the salinity in Fig. 2c. The transport contributions on the vertical axis are now plotted on a log scale to be able to compare the processes in the entire domain. It is clear that Chatwin's balance still dominates the dynamics in most of the estuary, except at the salt intrusion limit ( $x > 140$  km or  $s < 2$  psu at the bed). In this region, the balance shifts to a new complex balance which is dominated by import due to  $T_{gc-gc}$  and export due to the

covariance of velocity and salinity due to gravitational forces and momentum advection  $T_{adv-gc}$ . Additionally,  $T_{adv-adv}$  results in an important importing contribution, and  $T_{gc-riv}$  results in a smaller yet significant exporting contribution.

It was already shown above that  $T_{adv-gc}$  and  $T_{adv-adv}$  may tend to infinity at the salt intrusion limit given the Chatwin solution. To see when these momentum advection transport terms dominate over the dispersive transport, we compare their typical scales using  $\bar{s}$  and  $\bar{s}_x$  from the Chatwin solution. This yields

$$\frac{T_{adv-gc}}{T_{dispersion}} \sim \sigma_\rho^{-1/3} F_r^{4/3} Ra \Sigma^{1/3},$$

$$\frac{T_{adv-adv}}{T_{dispersion}} \sim \sigma_\rho^{-1} F_r^2 Ra.$$

Hence,  $T_{adv-gc}$  and  $T_{adv-adv}$  dominate over  $T_{dispersion}$  for large estuarine Froude numbers (i.e., relatively large discharge) or large estuarine Rayleigh numbers (i.e., relatively little mixing). For the particular cases illustrating regime 2 and 3 here, both  $F_r$  and  $Ra$  were increased. Only when  $\Sigma$  approaches 0 very closely does the dispersion term become dominant again, as can be seen in Fig. 3c.

The transport by  $T_{adv-gc}$  is always negative and therefore reduces salt intrusion relative to the Chatwin solution. The effect is a steepening of the along-channel salinity profile. This leads to locally larger salinity gradients at the salt intrusion limit, which leads to an increased import by  $T_{gc-gc}$  (which scales as  $\bar{s}_x^3$ ) and an even larger increase of the export by  $T_{adv-gc}$  (scales as  $\bar{s}_x^5$ ). This leads to an even further steepening of the salinity profile. We thus find a positive feedback between  $T_{gc-gc}$  and  $T_{adv-gc}$  that leads to the formation of a front-like salinity profile. This positive feedback is stopped when  $T_{adv-adv}$  becomes a significant importing mechanism. It scales with  $\bar{s}_x^7$  and balances the steepening effect of  $T_{adv-gc}$ . This feedback only occurs locally at the salt intrusion limit and explains why the balance of salt transport mechanisms is so strongly different from the balance in the rest of the estuary.

The local steepening of the salinity profile is also clearly visible in the decomposition of the horizontal velocity (Fig. 3d). Near the salt intrusion limit, the gravitational circulation peaks in a region of only a few kilometers. The velocity associated with momentum advection also shows such a peak and is oppositely directed to the gravitational circulation. As a result, the local steepening of the salinity profile is not reflected in the total subtidal velocity, as is shown in the right panel of Fig. 3d. Instead, the velocity field closely resembles that found in the example illustrating regime 2 (Fig. 2d). The effect of momentum advection is thus to oppose the formation of spatially localized peaks in the velocity profile, acting as a spatial equivalent to local inertia.

For other parameter settings that correspond to regime 3 than our example in Fig. 3, it is possible that the dominant effect of advection is not just restricted to a small area near the salt intrusion limit but extends farther up-estuary (an example is shown in section 3c). In such cases, the salt intrusion length is

no longer similar to the Chatwin salt intrusion length but is closer to the length scale we will derive for regime 4 below.

#### 4) REGIME 4: SUBTIDAL SALT WEDGE REGIME

The fourth and final regime identified here is the subtidal salt wedge regime. A typical example is found by choosing  $Q = 12000 \text{ m}^3 \text{ s}^{-1}$  and  $A_\nu = 5 \times 10^{-4} \text{ m}^2 \text{ s}^{-1}$  ( $F_r = 0.28$ ,  $Ra = 14000$ ). Figure 4a shows that the surface water is almost entirely fresh, while the bottom salinity decreases gradually close to the mouth and then rapidly near the salt intrusion limit. The result is a salinity front and a salt profile in the form of a classical subtidal salt wedge, which can be clearly seen in Fig. 4b. Figure 4a also shows the depth-mean salinity compared to the Chatwin solution (black dotted line). The Chatwin solution shows salt intrusion up to 90 km, while the fully non-linear model results in a salinity intrusion around 30 km. Clearly, the Chatwin solution is no longer a good approximation for the salt intrusion length.

The main transport contributions governing the salt wedge regime are shown in Fig. 4c. Similar to the case of regime 3, the  $y$  axis is plotted in log scale because the normalized transport contributions vary by several orders of magnitude throughout the estuary. The characteristic feature of regime 4 is that  $T_{gc-gc}$ ,  $T_{adv-gc}$ , and  $T_{adv-adv}$  are not only dominant near the salt intrusion limit but everywhere in the estuary. Both the transport related to dispersive effects and river flushing contribution are considerably smaller in the entire estuary. Accordingly, we define regime 4 as the regime where the transport contributions related to momentum advection are larger than the effects of dispersion and flushing in the entire estuary seaward of the salinity front. The balance of salt transport mechanisms can be intuitively understood as an extrapolation of the trend observed in regime 3. As the estuarine parameters are changed such that the along-channel salinity gradient becomes larger, the gravitational and momentum advection contributions increase and dominate the dispersion and river flushing contributions in an increasing part of the estuary, until the entire estuary is dominated by these terms in regime 4.

As the balance of processes now consists of at least four contributions of similar magnitude at any place in the estuary, it is unlikely to find an analytical expression for the salt intrusion length  $L_s$  from the scales of the individual terms. Instead using a two-layer model, Schijf and Schönfeld (1953) derived an analytical expression for salt intrusion length in salt wedge estuaries, which reads as

$$L_s = \frac{H}{4k} \left( \frac{1}{5} F_{r,2\text{-layer}}^{-2} - 2 + 3 F_{r,2\text{-layer}}^{2/3} - \frac{6}{5} F_{r,2\text{-layer}}^{4/3} \right).$$

This expression includes an estuary Froude number  $F_{r,2\text{-layer}}$ , which is defined differently from our  $F_r$ , and a friction coefficient  $k$  that measures the friction at the interface between the layers. We estimate  $F_{r,2\text{-layer}} = F_r/0.6$  (see appendix B for the definition of  $F_{r,2\text{-layer}}$  and the derivation of this relation). The friction coefficient cannot be uniquely related to the eddy viscosity used in our model. Nevertheless, by relating the shear stress in the two-layer model to the shear stress in our non-linear model, and assuming that the gravitational circulation is the main flow component at the mouth, we obtain an estimate

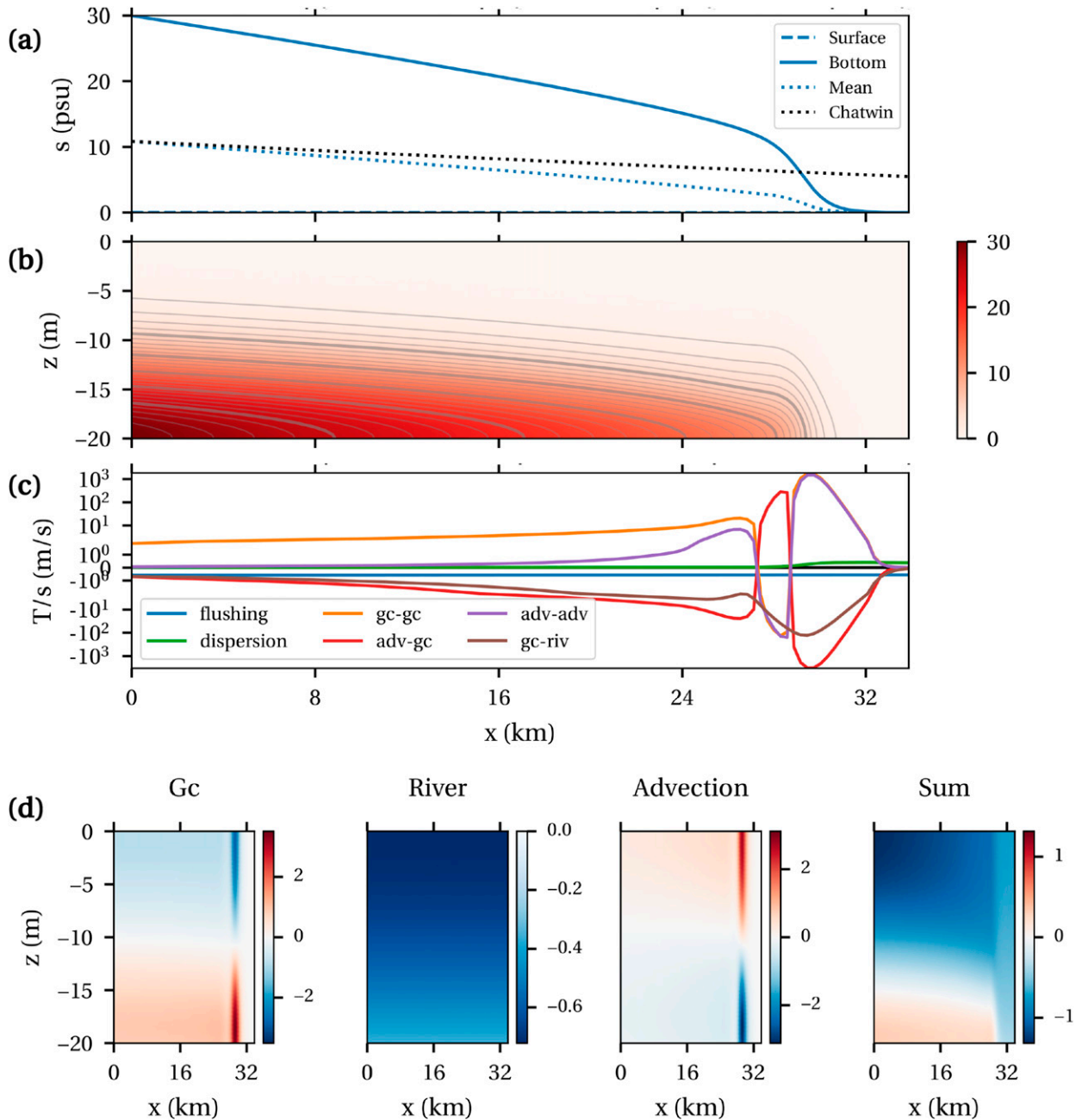


FIG. 4. As in Fig. 1, but for a case illustrating regime 4 using  $F_r = 0.28$ ,  $Ra = 14000$ .

for  $k$  (see appendix B for the derivation). This leads to the following estimated relation for the salt intrusion length scale

$$L_s \sim 0.07 \frac{H^{5/2} g^{1/2} \beta^{1/2}}{A_v} s_{(x=0)}^{1/2} \sqrt{0.072 F_r^{-2} - 2 + 4.2 F_r^{2/3} - 2.4 F_r^{4/3}}. \quad (40)$$

For the present case, this relation provides an estimate of the salt intrusion length  $L_s$  of 39 km, which is at least of the correct order of magnitude compared to the modeled salt intrusion

length of approximately 30 km. In section 4 we will further verify that this relation is a reasonable approximation for other cases in regime 4. It should be stressed, however, that this is a semi-empirically derived approximation, not an exact solution and should therefore be used with caution.

A striking feature in Fig. 4c is the reversal of the three most important transport contributions between 27 and 28 km, which turns out to be an artifact of the decomposition. The vertical velocity contributions associated with gravitational circulation and momentum advection become so large near the toe of the salt wedge that they locally invert the vertical salinity

shear associated with gravitational circulation  $s'_{gc}$  and momentum advection  $s'_{adv}$ . This causes the related transport contributions to invert as well. However, the total vertical velocity remains moderate and the total salinity remains stably stratified. Clearly, the local reversal of the transport contributions has no interpretation other than to note that the classical formulations of gravitational circulation and gravitational salinity shear in the sense of Hansen and Rattray (1965) and MacCready (2004) are not representative of the total exchange flow. Consequently, the typical scaling laws derived for gravitational circulation do not apply to the salt wedge regime.

*b. Regimes in parameter space*

The four cases presented above are typical examples observed in the four regimes. However, as one moves through the estuarine parameter space, gradual transitions between the four regimes are found. Therefore, to classify the entire parameter space, we performed a systematic sensitivity study. Values of  $F_r$  were varied between  $10^{-4}$  and 2, corresponding to river-induced velocities between  $\mathcal{O}(10^{-4})$  and  $\mathcal{O}(1)$  m s $^{-1}$ , which covers the typical range of velocities found in estuaries. To determine the range of values of Ra, we assumed typical values of  $A_v$  between  $10^{-4}$  and  $10^{-1}$  m $^2$  s $^{-1}$ ,  $K_h$  between  $10^2$  and  $10^4$  m $^2$  s $^{-1}$ , and  $H$  between 5 and 15 m. As a result Ra is between  $10^{-2}$  and  $7 \times 10^4$ . We do not show results for  $Ra < 25$  as these can be easily inferred from results with  $Ra = 25$ . The ranges for  $F_r$  and Ra are obtained by varying  $Q$  and  $A_v$  for fixed  $H$  and  $K_h$ , resulting in over 3000 model configurations. The main salinity transport contributions are determined from the results of each configuration and used to assign each configuration a decimal score between 1 and 4 to indicate the regime. The procedure for assigning this score is discussed in appendix C.

Figure 5 shows the resulting regimes as a function of the dimensionless parameters  $F_r$  and Ra. The black contour lines indicate regime score values of 1.5, 2.5, and 3.5 and may be considered the transition between the different regimes. Two of these lines run diagonally through the entire parameter space and divide the regimes 1, 2, and 3–4. Regime 1 is typically found for small Ra (i.e., large eddy viscosity or dispersion parameter) and small  $F_r$  (i.e., small freshwater discharge), but may also be found for large values of  $F_r$  if there is sufficient mixing. Regime 2 occupies a large range of moderate values of Ra and  $F_r$ . The area for regimes 3–4 is subdivided by an almost horizontal line, with regime 4 characterized by larger  $F_r$  than regime 3. The largest sensitivity of the salinity regime to  $F_r$  and Ra is found in the upper part of the figure for intermediate values of Ra and large values of  $F_r$ , where a transition between the regimes 1, 2, and 4 may occur for relatively small changes in  $F_r$  or Ra.

As shown in section 2e, the nonlinear model may be formulated entirely in terms of the two independent parameters  $F_r$  and Ra. Hence, the regimes shown in Fig. 5 also apply to any other parameter choices that results in the same values of  $F_r$  and Ra. The parameters  $F_r$  and Ra thus provide sufficient information to classify the entire parameter space based on the dominant processes or regimes. This has also been verified numerically by testing the model with values of  $H$  and  $K_h$  different from those used in our default case.

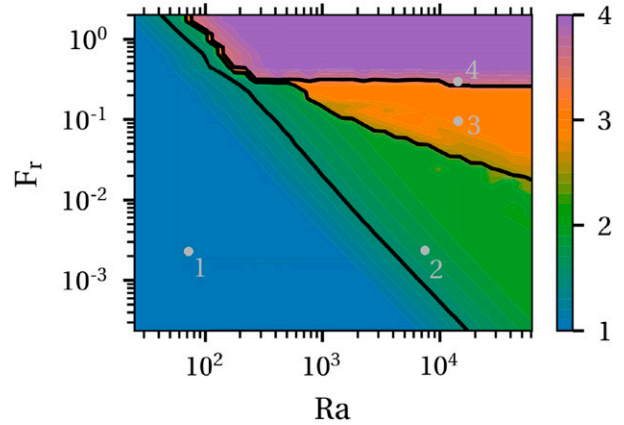


FIG. 5. Model results of regimes 1–4 plotted as a continuum in the parameter space of the freshwater Froude number  $Fr_f$  and Rayleigh number Ra. The colors indicate the regime. Black contour lines mark the transitions between the regimes. The gray dots indicate the location of the examples plotted in Figs. 1–4.

Analytical approximations of the lines separating the regimes may be obtained. At the transition between regime 1 and 2 the salt intrusion length of the dispersive balance (regime 1) and the Chatwin balance (regime 2) become of similar magnitude. Equating the expressions for  $L_s$  from regimes 1 and 2 [Eqs. (36) and (39)], we obtain an expression for the line dividing the regimes. Expressed in terms of  $F_r$  and Ra this yields

$$F_r \sim \sigma_\rho^{-1/2} Ra^{-3/2} \Sigma_{x=0}^{-1} \text{ (division regime 1–2)}. \quad (41)$$

We have used  $\sim$  in this expression to indicate proportionality. The constant of proportionality should follow from fitting to the numerical results. We do not provide a specific value here, as this value depends on details, such as the choice of a no-slip versus partial slip bottom boundary condition or the relation between friction and eddy viscosity. Regardless of this choice, the proportionality remains valid and this is what we want to emphasize. Hence, the most important result is that the division between regimes 1 and 2 scales as  $F_r \sim Ra^{-3/2}$ , which is also found approximately in our model results in Fig. 5.

The transition between regime 2 and 3 occurs when  $|T_{dispersion}|$  and  $|T_{adv-gc}|$  become similarly important at the salt intrusion limit. Assuming the Chatwin solution for the salt intrusion length [Eq. (39)] holds and equating the expressions for  $T_{dispersion}$  and  $T_{adv-gc}$  from Eq. (30), we obtain

$$F_r \sim \sigma_\rho^{1/4} Ra^{-3/4} \Sigma^{-1/4} \text{ (division regime 2–3)}. \quad (42)$$

Again, the constant of proportionality should follow from fitting to the model results. The line dividing regimes 2 and 3 scales as  $F_r \sim Ra^{-3/4}$ , which also corresponds to our model results in Fig. 5.

Finally, regime 3 transitions into regime 4 when the salt intrusion length of the Chatwin solution [Eq. (39)] and the salt wedge solution [Eq. (40)] become of similar magnitude. Therefore, the line dividing regime 3 and 4 may be approximated by equating these two length scales, resulting in the implicit relation

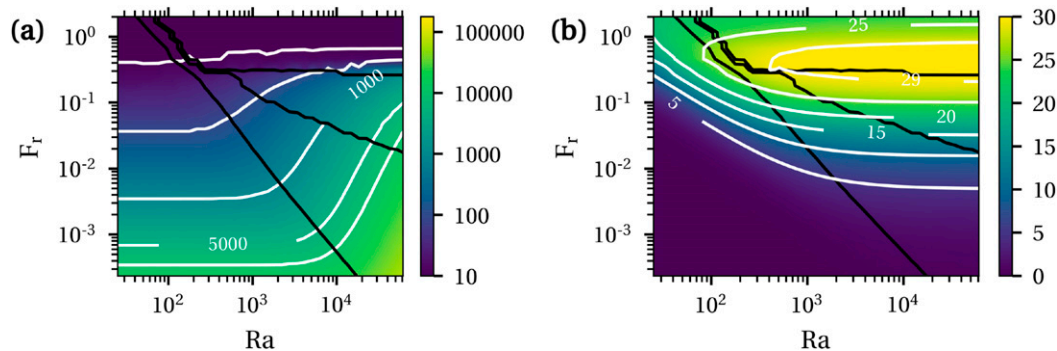


FIG. 6. (a) Dimensionless salt intrusion length and (b) maximum top–bottom stratification for various values of  $F_r$  and  $Ra$ . The black contour lines correspond to the transitions between the regimes from Fig. 5.

$$F_r^{1/3} \sqrt{0.072F_r^{-2} - 2 + 4.2F_r^{2/3} - 2.4F_r^{4/3}} \sim \sigma_p^{1/3} \Sigma_{x=0}^{1/6} \text{ (division regime 3–4)}. \quad (43)$$

This expression shows that the dividing line between regimes 3 and 4 does not depend on  $Ra$  at all, corresponding to the horizontal dividing line in Fig. 5 for sufficiently large  $Ra$ . The slopes of the lines dividing all four regimes can thus be understood from the balances of salt intrusion length scales and transport contributions and may be estimated analytically.

### c. Stratification and salt intrusion length

Next we investigate the relation between the identified mechanistic regimes and the salt intrusion length and top–bottom stratification. It is found that there is no unique relation between the actual salt intrusion length  $L_s$  (in m) and  $F_r$  and  $Ra$ . However, when instead considering the dimensionless salt intrusion length  $\mathcal{L}_s$  [see Eq. (34)] such a unique relation is found and the result is plotted in Fig. 6a. This figure additionally shows the lines distinguishing the regimes from Fig. 5. The lines of equal salt intrusion length are almost perpendicular to lines dividing regimes 1, 2, and 3. Clearly, the salt intrusion length provides very little information about the dominant physics (i.e., the regime) and vice versa. Only regime 4 is typically associated with relatively short salt intrusion length. This is because this regime is dominated by momentum advection, which acts as a form of spatial inertia and restricts the flow. It therefore prevents a sufficiently strong baroclinic inflow to balance the river discharge, hence restricting import of salt. On the top of the figure, for  $F_r$  approximately larger than 0.6, the salt wedge is expelled from the estuary and only the toe of the salt wedge remains, corresponding to a very short salt intrusion length.

The maximum subtidal top–bottom stratification  $\Delta s$  may also be expressed as a unique function of only  $F_r$  and  $Ra$  (Fig. 6b). The figure shows that there is also no strong relation between  $\Delta s$  and the regimes. Stratification anywhere between  $\Delta s = 0$  and  $\Delta s > 20$  psu may be found in regime 1, while regime 2 may see  $\Delta s$  varying between a few psu and almost 30 psu. Regime 3 is always characterized by a significant stratification but this may still vary from 10 psu to almost 30 psu. Only regime 4 is characterized by almost fully stratified conditions with  $\Delta s \approx 30$  psu, as long as  $F_r < 0.6$ . When the salt wedge is

expelled for  $F_r > 0.6$ , only the toe of the salt wedge remains in which the stratification is somewhat smaller than 30 psu. It is thus evident from this figure that the stratification structure, i.e., well-mixed, partially mixed, or strongly stratified, only has a weak relation with the mechanistic regime.

## 4. Discussion: Salt intrusion length as a function of discharge and depth

To better compare the results to results used in literature, we look closer at the dependency of the salt intrusion length and two specific observable parameters: the river discharge and depth. Literature provides a large number of expressions relating salt intrusion length to depth and discharge, often using power laws with various values of the powers based on regression analysis on observations or numerical model results (e.g., Monismith et al. 2002; Ralston et al. 2008; Haralambidou et al. 2010; Gong and Shen 2011; Aristizábal and Chant 2013; Chant et al. 2018). The large range of values for the powers found for different estuaries can partly be explained by spatial variations in bathymetry, geometry, and mixing, and partly by different salinity regimes (e.g., Ralston et al. 2010). Based on our results, we can describe the theoretically expected powers in each regime and in the transitions between these regimes assuming a spatially uniform estuary.

To this end, the salt intrusion length estimates for the four regimes in Eqs. (36), (39), and (40) are repeated, where possible omitting all parameter dependencies except for the dependency on  $Q$  and  $H$ . The resulting expressions read as

$$L_s \sim HQ^{-1} \text{ (regime 1)}, \quad (44)$$

$$L_s \sim H^3 Q^{-1/3} \text{ (regime 2)}, \quad (45)$$

$$L_s \sim H^{5/2} \left[ 0.072 \left( \frac{B}{gB s_{\text{sea}}} \right)^2 \frac{H^3}{Q^2} - 2 + 4.2 \left( \frac{gB s_{\text{sea}}}{B} \right)^{2/3} \frac{Q^{2/3}}{H} - 2.4 \left( \frac{gB s_{\text{sea}}}{B} \right)^{4/3} \frac{Q^{4/3}}{H^2} \right] \text{ (regime 4)}. \quad (46)$$

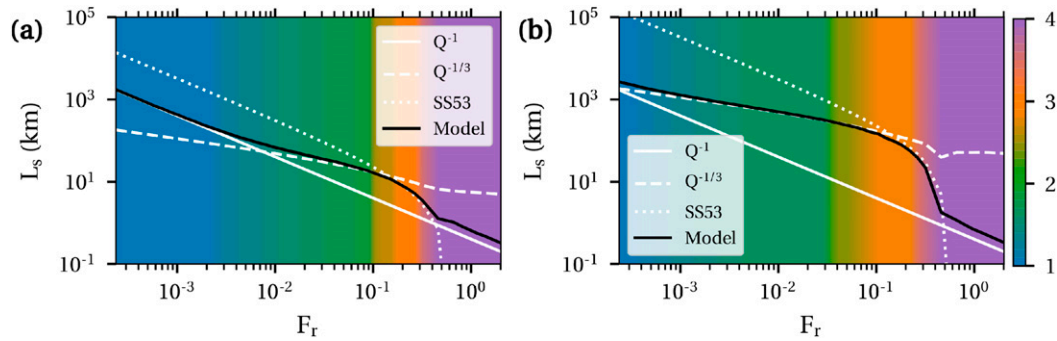


FIG. 7. Salt intrusion length as a function of the discharge for two different values of the eddy viscosity: (a)  $A_\nu = 0.005$  and (b)  $A_\nu = 0.0005$ . The black line shows the model result. The white lines show the theoretical solutions for regime 1 (solid), 2/3 (dashed), and 4 (dotted). The colors in the background indicate the regime using the color coding of Fig. 5.

Regime 3 is characterized by a transition between the length scales of regime 2 and 4. The expressions for regimes 1 and 2 correspond to those presented in Hansen and Rattray (1965), Monismith et al. (2002), and MacCready (2004). Recall that the expression for regime 4 does not directly follow from the model equations but is inspired by two-layer model results.

a. Scaling with discharge

Figure 7 shows the salt intrusion length according to Eqs. (36) (solid white line), (39) (dashed white line), and (40) (dotted white line) along with the model result of the salt intrusion length as a function of the discharge  $Q$  for the default settings and two different values of the eddy viscosity  $A_\nu$ . The colors in the background indicate the regime (see Fig. 5). For  $A_\nu = 0.005 \text{ m}^2 \text{ s}^{-1}$  (Fig. 7a), results are in regime 1 for approximately  $F_r < 7 \times 10^{-2}$  and correspondingly  $L_s$  follows the dispersive relation, which scales as  $Q^{-1}$ . As the results move into regime 2 for  $10^{-2} < F_r < 0.1$  the relation tends toward the Chatwin solution, scaling as  $Q^{-1/3}$ . However, it never quite attains this relation as the curve steepens when moving toward regime 3. For  $F_r > 0.1$ , where the solution moves from regime 3 to regime 4, the salt intrusion lengths tends toward the salt wedge solution but also never fully attains this solution. For approximately  $F_r > 0.6$ , the relation tends back to  $L_s \sim Q^{-1}$ . For these values of  $F_r$ , the salt wedge is expelled from the estuary and salt only remains inside the domain because the seaward boundary condition requires salt to be present. As it becomes unclear for such high discharges whether there should even be any salt inside the estuary, this should not be given any physical interpretation.

For  $A_\nu = 0.0005 \text{ m}^2 \text{ s}^{-1}$  (Fig. 7b), a larger range of values of  $Q$  result in a balance characteristic for regime 2. As a result, the model solution now closely approaches the Chatwin relation. Again, the relation between  $L_s$  and  $Q$  steepens moving into regimes 3 and 4 and the solution follows the salt wedge solution closely for  $0.2 < F_r < 0.6$ . For  $F_r > 0.6$  the solution again tends toward  $Q^{-1}$  as the salt is expelled from the estuary.

b. Scaling with depth

The estuary depth appears in both dimensionless parameters  $F_r$  and  $Ra$  as  $F_r \sim H^{-3/2}$  and  $Ra \sim H^{3/4}$ . As a result, a change in depth means that the solution moves along a line  $F_r \sim Ra^{-1/2}$ .

Relating this to Fig. 5 shows that a change in depth leads to a change almost parallel to the line separating regimes 2 and 3. This means that an estuary in regime 1 or 2 will not likely change to regime 3 or 4 if only the depth is changed and vice versa (note that all other parameters, including the eddy viscosity, remain unchanged).

We have, however, already seen that the regime provides little information about the salt intrusion length. Therefore, it remains interesting to investigate the relation between the salt intrusion length, depth, and regime. Figure 8 shows the relation between the salt intrusion length and the depth for two cases. Figure 8a shows results for  $Q = 1000 \text{ m}^2 \text{ s}^{-1}$  and  $A_\nu = 0.005 \text{ m}^2 \text{ s}^{-1}$ . For  $H < 10 \text{ m}$ , the regime is predominantly dispersive and the salt intrusion length scales as  $L_s \sim H$ , following the dispersive relation (white solid line). For  $H > 20 \text{ m}$ , the Chatwin regime predominates and  $L_s$  scales as  $H^3$  (white dashed line). The figure additionally confirms that the solution remains within regime 1–2 and does not cross into regime 3 or 4. Figure 8b shows results for  $Q = 10000 \text{ m}^2 \text{ s}^{-1}$  and  $A_\nu = 0.0005 \text{ m}^2 \text{ s}^{-1}$ . Small depths now correspond to regime 4, while larger depths ( $H > 15$ ) result in regime 3. The simulations remain in regime 3–4 and do not move to regime 2. In most of regime 4, the salt intrusion is a few kilometers at most and the solution behaves similar to a dispersive solution with  $L_s \sim H$ . This corresponds to an expelled salt wedge as identified above and should not be given any physical interpretation. When  $H > 12 \text{ m}$ , the salt intrusion length increases and starts to follow the theoretical two-layer solution (white dotted line). For  $H > 19 \text{ m}$ , the solution behaves entirely according to regime 3 and follows the Chatwin solution with  $L_s \sim H^3$ .

c. Application to real estuaries

To apply this theoretical framework to real estuaries, the typical values of  $Ra$  and  $F_r$  need to be estimated. To determine these numbers, most parameters may be estimated quite easily. However, the eddy viscosity and dispersion parameter  $K_t$  are not directly observable and there is no unambiguous procedure for determining these parameters for a given estuary. An easier way of classifying estuaries by observable parameters is, for example, using the parameters introduced by Hansen and Rattray (1966): the circulation and stratification. The circulation is defined as the subtidal surface velocity divided by the

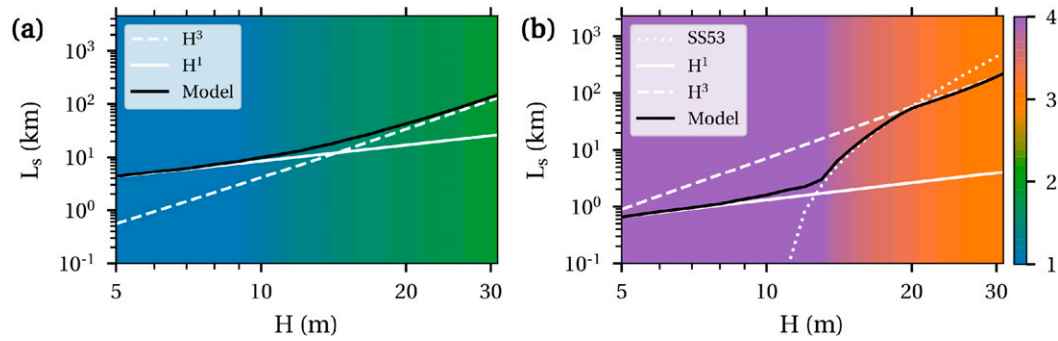


FIG. 8. Salt intrusion length as a function of the depth illustrated for two different values of the eddy viscosity and discharge: (a)  $A_v = 0.005 \text{ m}^2 \text{ s}^{-1}$ ,  $Q = 1000 \text{ m}^3 \text{ s}^{-1}$  and (b)  $A_v = 0.0005 \text{ m}^2 \text{ s}^{-1}$ ,  $Q = 10000 \text{ m}^3 \text{ s}^{-1}$ . The black line shows the model result. The white lines show the theoretical solutions for regime 1 (solid), 2/3 (dashed), and 4 (dotted). The colors in the background indicate the regime using the color coding of Fig. 5.

depth-averaged velocity. The stratification is defined as the subtidal top–bottom salinity difference divided by the depth-averaged salinity. We found there is an injective mapping between the parameters  $Ra$  and  $F_r$  and the circulation and stratification within the context of our model (i.e., every  $Ra$ – $F_r$  pair corresponds uniquely to one circulation–stratification pair). The mapping is computed numerically using the model.

The resulting classification of several estuaries using this method is presented in Fig. 9. For several estuaries, we have plotted the regime under low and high discharge conditions, indicated by subscripts l and h, respectively. For the Delaware, James, and Rotterdam waterway we have plotted a line indicating the regime along a section in the interior part of the estuary (see appendix D for details). It is important to remember that observed circulation and stratification reflect effects of tides, lateral circulation, and other flow contributions that are parameterized in our simple model. Such contributions may be incorrectly identified here as caused by, e.g., gravitational circulation, leading to inaccurate estimates of  $Ra$  and  $F_r$ . This classification should therefore be regarded as indicative and understood within the context and limitations of the model. Moreover, as bathymetry and mixing parameters are not along-channel uniform in real estuaries, different parts of the estuary have different representative  $Ra$  and  $F_r$  values and thus may behave according to different regimes (see, e.g., the examples given by MacCready 2004). If variations occur on short along-channel length scales, topographic effects may alter the salinity structure (Geyer and Ralston 2015) and these are not captured using our theory. Furthermore, forcing conditions are not constant in time, leading to time variations of  $Ra$  and  $F_r$  and an estuary may be in different regimes at different times. It should be taken into account though that our theory assumes a steady state and is therefore only applicable for gradually changing conditions on time scales longer than the typical adjustment time scale (see, e.g., MacCready 2007).

Despite the indicative nature of Fig. 9, we find that estuaries that are usually regarded as partially stratified, including the Hudson, Delaware, and James Rivers (e.g., Geyer and MacCready 2014) are in regime 2, corresponding to our expectation based on Chatwin (1976). The well-mixed Scheldt estuary is in regime 1 as expected. Regime 1 additionally

features the Rotterdam waterway, Columbia River (high discharge), and Mississippi River (high discharge). These are systems that display temporally varying strong stratification with a dominant effect of tides. The complex dynamics of these estuaries is not captured using our subtidal model but the classification rightly identifies that (tidal) dispersion is dominant. The Hudson estuary at high discharge is also associated to be a tidally dependent strongly stratified estuary (e.g.,

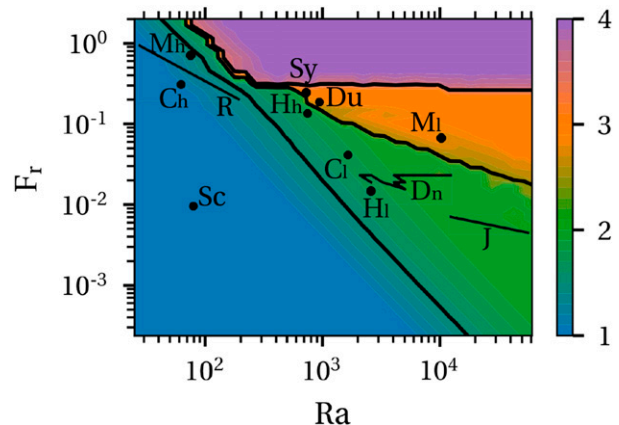


FIG. 9. Indicative location of several estuaries in the parameters space based on observed stratification and circulation. Dots denote single locations in the estuary, while lines denote an along-channel stretch of the estuary. These examples are derived based on published observations of model results. The letters indicate: C: Columbia (United States), D: Delaware (United States), Du: Duwamish (United States), H: Hudson (United States), J: James (United States), M: Mississippi (United States), R: Rotterdam Waterway (branch of the Rhine–Meuse delta, Netherlands), Sc: Scheldt (Belgium), Sy: Strymon (Greece). Subscripts ‘l’ and ‘h’ denote low and high river discharges, respectively. Subscript ‘n’ denotes neap conditions. Note that the locations of these examples are only valid approximately and may vary with flow conditions and use of data at different locations along the length and cross section of the estuary. Additionally, as obtaining subtidal quantities in tidal environments is error prone, the data or models used to plot these examples may be inaccurate. The reader is referred to appendix D for details on how these examples were derived.

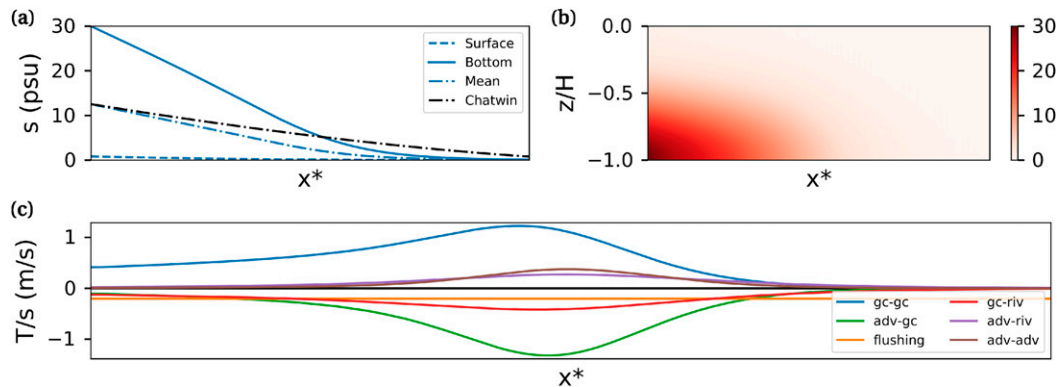


FIG. 10. Model results for the parameters  $Ra = 900$ ,  $Fr = 0.17$ , representative of the Strymon River. (a) Salt intrusion at the bottom, surface, and depth-averaged compared to the salt intrusion in the Chatwin limit. (b) along-channel profile of salinity. (c) Selection of most important salt transport mechanisms. The  $x$  axis represents dimensionless along-channel distance and contains no numbers to emphasize that salt intrusion length may vary with chosen parameter values.

Ralston et al. 2008) but nevertheless classified in regime 2. It is unclear if this is correct, and it is likely that some of the tidally generated exchange flow is incorrectly identified as gravitational circulation. Moreover, it is located in a part of the parameter space where all regimes are close together and the exact classification is sensitive to variations in classification methodology and variations in observations.

None of the estuaries in Fig. 9 are in regime 4. This is not entirely surprising as the subtidal top–bottom salinity difference in regime 4 equals the maximum salinity at least at one location. Almost any mixing that may occur during any part of the tidal cycle reduces the salinity difference below this. Nevertheless, the strongly stratified, microtidal Strymon River (Greece) in regime 3 has many of the characteristics of a typical regime 4 estuary, as shown in Fig. 10. The salinity structure resembles that of a salt wedge (Fig. 10b) and the salt intrusion length (Fig. 10a) is much shorter than the Chatwin salt intrusion length. Figure 10c correspondingly shows that momentum advection and gravitational circulation are dominant in most of the estuary. The Chatwin balance dominates only in the seaward-most part of the estuary, which puts this estuary in regime 3 (according to our mechanistic definition) but with most of the characteristics of regime 4.

### 5. Conclusions

We have investigated the dynamics driving the salt intrusion in estuaries ranging from well-mixed to salt wedge estuaries in the context of a steady subtidal width-averaged model. Thereby we provide a unifying approach that links the classical subtidal width-averaged models for well-mixed, partially mixed, and salt wedge estuaries. We have identified four regimes, based on different main balances of physical mechanisms. These regimes and their dominating mechanisms are

- 1) *dispersive regime*: a balance between transport due to (tidal) dispersion and river-induced flushing;
- 2) *Chatwin regime*: a balance between vertical shear dispersion due to gravitational circulation and river-induced flushing. At the salt intrusion limit, the balance changes back to the dispersive balance;

- 3) *Chatwin regime with advection dominated front*: similar to the Chatwin regime in most of the estuary. However, momentum advection leads to the formation of a salinity front at the salt intrusion limit, accompanied by strong salinity gradients;
- 4) *subtidal salt wedge regime*: a balance between vertical shear dispersion due to gravitational circulation and effects of momentum advection.

Regimes 1 and 2 were already identified by Hansen and Rattray (1965), Chatwin (1976), and MacCready (2004). Regimes 3 and 4 are newly identified in this study and are shown to be dominated by the effects of momentum advection, which was not considered by the aforementioned authors. The importance of momentum advection in a subtidal salt wedge corresponds to earlier findings by, e.g., Schijf and Schönfeld (1953). Momentum advection acts as spatial inertia, restricting the exchange flow in steep subtidal salinity fronts and limiting the subtidal salt intrusion length. For each regime, we have derived expressions for the salt intrusion length in terms of estuarine parameters. It is shown that the salt intrusion length scales derived for regime 1 and 2 by Chatwin (1976) and MacCready (2004) are good approximations, even though they are derived from a much simpler quasi-nonlinear model. The salt intrusion length scale for regime 2 is additionally applicable in a significant part of regime 3. In the rest of regime 3 and regime 4, the salt intrusion length scale derived by Schijf and Schönfeld (1953) is a good approximation. Thus, regime 3 should be regarded as a transition regime between regimes 2 and 4.

The salinity regime in a particular estuary can, within the context of our model, be explicitly determined using two dimensionless parameters: the estuarine Froude number  $F_r$ , measuring the freshwater discharge, and the estuarine Rayleigh number  $Ra$ , measuring the amount of mixing. These two parameters furthermore determine the maximum subtidal vertical salinity stratification and the dimensionless salt intrusion length. The dimensional salt intrusion length scales differently and can thus assume different values for the same  $F_r$  and  $Ra$ . By relating  $Ra$  and  $F_r$  to more easily observable parameters related to stratification and circulation, the location of several estuaries in the parameter space could be estimated.

Estuaries were found across the parameter space; however, it seems there might be no estuaries entirely satisfying the conditions for regime 4. Nevertheless, estuaries are found in regime 3 that resemble the typical characteristics in regime 4.

Within each regime, the salt intrusion length and stratification may vary strongly, depending on the value of the estuarine parameters. Although stratification typically increases from regime 1 to regime 4, moderate top–bottom salinity difference of 10–20 psu may occur in regime 1, 2, and 3. Additionally, almost any salt intrusion length may be attained in regime 1, 2, or 3. Only regime 4 is always characterized by a top–bottom salinity difference of 30 psu and restricted salt intrusion length, controlled by momentum advection. Stratification and salt intrusion length therefore provide only very limited information about the governing processes and cannot be directly linked to the salinity regime.

*Acknowledgments.* This research was funded by the Dutch Science Organisation (NWO, Grant ALWSD.2016.015).

## APPENDIX A

### Scaling of the Transport Contributions

Equation (30) presents the scaling of the salt transport contributions with the model parameters. For the velocity and salinity shear contributions related to the river discharge and baroclinic pressure, these scales follow from analytical solutions to the reduced Eqs. (18)–(21) and (24)–(25) with the additional assumption that  $s_x$  may be represented by a depth-average  $\bar{s}_x$ . The resulting analytical solutions read as

$$u_{\text{riv,analytical}} = -\frac{Q}{BH} \frac{R + \frac{1}{2} - \frac{1}{2}\sigma^2}{R + \frac{1}{3}}, \quad (\text{A1a})$$

$$u_{\text{gc,analytical}} = -\frac{gBH^3}{A_\nu} \bar{s}_x \left[ \left( \frac{1}{2}\sigma^2 - \frac{1}{2} - R \right) \frac{\frac{1}{8} + \frac{1}{2}R}{R + \frac{1}{3}} + \frac{1}{6}(\sigma^3 + 1) + \frac{1}{2}R \right], \quad (\text{A1b})$$

$$s'_{\text{riv,analytical}} = \frac{QH^2}{AK_\nu} \bar{s}_x \frac{\frac{1}{24}\sigma^4 - \frac{1}{12}\sigma^2 + \frac{7}{360}}{R + \frac{1}{3}}, \quad (\text{A1c})$$

$$s'_{\text{gc,analytical}} = -\frac{gBH^5}{A_\nu K_\nu} \bar{s}_x \left\{ \frac{1}{120}\sigma^5 + \frac{1}{24} \frac{\frac{1}{8} + \frac{1}{2}R}{R + \frac{1}{3}} \sigma^4 + \left[ \frac{1}{12} + \frac{1}{4}R - \left( \frac{1}{4} + \frac{1}{2}R \right) \frac{\frac{1}{8} + \frac{1}{2}R}{R + \frac{1}{3}} \right] \sigma^2 + \frac{1}{8640} \frac{5 + 36R}{R + \frac{1}{3}} \right\}. \quad (\text{A1d})$$

where  $\sigma = z/H$  and  $R = A_\nu/s_\nu H$ . These expressions are identical to those appearing in MacCready (2004) when using  $R = 0$ . These expressions are used to compute the contributions to the cross-sectionally averaged transport  $(1/H) \int_{-H}^0 us' dz$ . The transport contributions (30a)–(30e) are obtained by using our assumption  $R = 1/2$  [see Eq. (15)].

The contributions associated with momentum advection are estimated by assuming that the right-hand side of Eq. (22) is dominated by  $u_{\text{gc,analytical}} u_{\text{gc,analytical},x}$  and the right-hand side of Eq. (26) is dominated by  $u_{\text{adv,analytical}} \bar{s}_x$ . The resulting equations may be solved analytically to obtain

$$u_{\text{adv,analytical}} = \gamma_1(R) \frac{g^2 \beta^2 H^8}{A_\nu^3} \bar{s}_x \bar{s}_{xx}, \quad (\text{A2a})$$

$$s'_{\text{adv,analytical}} = \gamma_2(R) \frac{g^2 \beta^2 H^{10}}{A_\nu^3 K_\nu} \bar{s}_x^2 \bar{s}_{xx}, \quad (\text{A2b})$$

with coefficients  $\gamma_1$  and  $\gamma_2$  depending on  $R$ . These expressions are used to compute the contributions to the cross-sectionally averaged transport associated with momentum advection (30f)–(30h). As the above velocity and salinity contributions are only approximations, we ignore the values of  $\gamma_1$  and  $\gamma_2$  in determining the magnitude of these transport contributions. Instead the coefficients of the advective terms are derived numerically from the results of the model experiments by taking the maximum and minimum order of magnitude in the parameter space.

## APPENDIX B

### Salt Intrusion Length for Regime 4

To derive an approximate expression for the salt intrusion length for the salt wedge regime, we start from the two-layer solution of Schijf and Schönfeld (1953), repeated for convenience

$$L_s = \frac{H}{4k} \left( \frac{1}{5} F_{r,2\text{-layer}}^{-2} - 2 + 3F_{r,2\text{-layer}}^{2/3} - \frac{6}{5} F_{r,2\text{-layer}}^{4/3} \right). \quad (\text{B1})$$

This expression contains two parameters that need to be related to our model experiments:  $F_{r,2\text{-layer}}$  and  $k$ . The Froude number  $F_{r,2\text{-layer}}$  is defined as  $\sqrt{\rho[(\rho_2 - \rho_1)gH]}(Q/BH)$ , where  $\rho_1$  and  $\rho_2$  are the densities of the upper and lower layer, respectively. When converting this model to a continuous model like the one used in this study, the densities  $\rho_2$  and  $\rho_1$  are unclear. Therefore, we choose a pragmatic approach and relate  $F_{r,2\text{-layer}}$  to  $F_r$  by observing the point where the salt wedge is expelled from the estuary. This is for  $F_{r,2\text{-layer}} = 1$  in the above equation and for  $F_r \approx 0.6$  in our model.

The friction coefficient  $k$  is defined from the shear stress at the interface between the two layers. In our continuous model this definition reads as

$$\tau/\rho = ku^2 = A_\nu u_z.$$

We concentrate on the estuary mouth and estimate that the velocity is dominated by  $u_{\text{gc}}$ . Furthermore, we scale  $u_z$  as  $u/H$ . We then find

$$k \sim \frac{A_\nu}{u_{\text{gc}} H}.$$

Using the expression for  $u_{gc}$  from [appendix A](#) and assuming that the salinity gradient scales as the salinity at the mouth divided by the salt intrusion length, we find

$$k \sim 48Ra^{-2} \mathcal{L}_s \sum_{(x=0)}^{-1} \frac{cH}{K_h}$$

Substituting this in Eq. (B1) and rewriting yields our estimate for  $L_s$  for a salt wedge.

### APPENDIX C

#### Procedure for Assigning a Regime

To emphasize that the four regimes are a continuum, we assign a regime to each case using a decimal number between 1 and 4. There are many ways to define such a regime score. We developed an algorithm that stays close to our interpretation of the regimes, by making indicators that measure the most important characteristics to define the transition between the regimes. To score the transition between regime 1 and 2 we measure the average importance of  $T_{gc-gc}$  (regime 2) compared to  $T_{dispersion}$  (regime 1) as

$$\text{score}_{1-2} = \frac{1}{L_s} \int_0^{L_s} \frac{T_{gc-gc}}{T_{dispersion}}, \quad (C1)$$

where  $L_s$  is the salt intrusion length defined such that  $s(L_s, -H) = 1$  psu. The transition between regime 2 and 3 is scored by measuring the importance of  $|T_{adv-gc}|$  (regime 3) relative to  $T_{dispersion}$  (regime 2) at the point  $x_{front}$  where  $|T_{adv-gc}|$  attains its maximum value, i.e.,

$$\text{score}_{2-3} = \frac{|T_{adv-gc}|(x_{front})}{T_{dispersion}(x_{front})}, \quad (C2)$$

Regime 4 is scored by measuring the smallest value of advection-related transport (regime 4) relative to flushing and dispersion (regime 3) in any point before the salinity front, i.e.,

$$\text{score}_{3-4} = \min_x \left( \frac{|T_{adv-gc}| + |T_{adv-adv}|}{|T_{flushing}| + |T_{dispersion}|} \right) \text{ for } x < x_{front}. \quad (C3)$$

The values of these scores are truncated at values 0.1 and 10, i.e., values at which either the mechanisms in the numerator is 10 times weaker or stronger than the mechanism in the denominator. As a result the expression  $[\log_{10}(\text{score}_i) + 1]/2$  ( $i = 1-2, 2-3, 3-4$ ) ranges between 0 and 1. The regime is then determined as

$$\left\{ \begin{array}{ll} 3 + \frac{\log_{10}(\text{score}_{3-4}) + 1}{2} & \text{if } \text{score}_{3-4} > 0.1 \text{ and } \\ & \text{score}_{2-3} > 5, \text{ else,} \\ 2 + \frac{\log_{10}(\text{score}_{2-3}) + 1}{2} & \text{if } \text{score}_{2-3} > 0.1 \text{ and } \\ & \text{score}_{1-2} > 5, \text{ else,} \\ 1 + \frac{\log_{10}(\text{score}_{1-2}) + 1}{2} & \text{if } \text{score}_{1-2} > 0.1, \text{ else,} \\ 1. & \end{array} \right. \quad (C4)$$

The first condition sets regimes in the range between 3 and 4 on the basis of  $\text{score}_{3-4}$ , provided that  $\text{score}_{2-3}$  is at least sufficiently large. Otherwise, condition 2 sets regimes between 2 and 3 on the basis of  $\text{score}_{2-3}$  etcetera. Values exactly between the regimes (i.e., 1.5, 2.5, 3.5) are attained when the two mechanisms that define the regimes are exactly equal. For example, for regime 1.5, the average dispersive and gravitational transport are exactly equal.

### APPENDIX D

#### Location of Estuaries in the Parameter Space

[Figure 9](#) shows the location of several estuaries in the parameter space. These locations have been derived on the basis of observations and model results of stratification and circulation published by others. The stratification and circulation were then converted numerically to values of  $Ra$  and  $F_r$ , yielding corresponding stratification and circulation in our model. Below is a summary of the data used and the way stratification and circulation were determined for each plotted estuary. The Columbia, James and Mississippi are not mentioned below: these examples have been copied directly from the circulation and stratification given by [Hansen and Rattray \(1966\)](#).

##### a. Delaware

Stratification and circulation in the Delaware were based on 3D model results presented by [Aristizábal and Chant \(2013\)](#) for the case  $Q = 650 \text{ m}^3 \text{ s}^{-1}$  and neap tidal conditions. We show results between 30 and 50 km, in the middle part of the estuary. The top-bottom salinity difference along the thalweg is presented in their Fig. 13b and the mean salinity is plotted in their Fig. 14a. Additionally they compute values of  $\nu$  based on their model results. We have used the combination of the stratification and parameter  $\nu$  to infer the circulation using the model of [Hansen and Rattray \(1966\)](#). Note that salinity data are based on results along the thalweg, while  $\nu$  is computed based on cross-sectionally integrated salt transport.

##### b. Duwamish

Data for the Duwamish were derived from [McKeon et al. \(2020\)](#) for a river discharge of  $65 \text{ m}^3 \text{ s}^{-1}$  at a location 7.5 km from the mouth. They present subtidal velocity profiles in their Fig. 4. The surface velocity was derived from this figure, while the average velocity was determined by dividing the river discharge by the local cross-sectional area. The stratification was estimated from ebb and flood salinity in their Fig. 4.

##### c. Hudson

Data for the Hudson were taken from [Ralston et al. \(2008\)](#). They present observations of the time-averaged vertical velocity profile (their Fig. 8) to determine the surface velocity. The mentioned discharge and cross-sectional area are divided to determine the average velocity. The time-averaged top-bottom salinity is presented in their Fig. 6). The depth-averaged salinity is taken as the mean of the top and bottom salinities. Data are used for two discharge cases in the year

2004: low ( $400 \text{ m}^3 \text{ s}^{-1}$ , day 190) and high ( $2200 \text{ m}^3 \text{ s}^{-1}$ , day 92) at Hastings (33 km, mean salinity between 3 and 13 psu).

#### d. Rotterdam Waterway

Data were used from De Nijs et al. (2011) Fig. 2, which presents the vertical–temporal structure of the flow velocity and salinity observed on 11 April 2006. Discharges were above average ( $4400\text{--}5800 \text{ m}^3 \text{ s}^{-1}$  at Lobith). The data are time-averaged to find the subtidal circulation and stratification. Data at from station 1 ( $\sim 7$  km from the mouth) and 2 ( $\sim 18$  km) were used.

#### e. Scheldt

Top–bottom salinity data for the Scheldt were taken from the permanent measurement station at Boei 84 ( $\sim 60$  km) for the months January–May 2015 (Vanlierde et al. 2016). As stratification is small, the depth-averaged salinity is taken to equal the average of the top and bottom salinities. No reliable subtidal velocities are available and hence the circulation is based on only the river flow and gravitational circulation as computed by Brouwer et al. (2015). This may not equal the actual circulation as it may be observed but is consistent with the meaning of the circulation in our model.

#### f. Strymon

Observations by Haralambidou et al. (2010) were used. Their Fig. 2 presents vertical profiles of velocity and salinity measured in the summer of 2003 at 2 km.

### REFERENCES

- Aristizábal, M. F., and R. J. Chant, 2013: A numerical study of salt fluxes in Delaware Bay Estuary. *J. Phys. Oceanogr.*, **43**, 1572–1588, <https://doi.org/10.1175/JPO-D-12-0124.1>.
- Arita, M., and G. H. Jirka, 1987: Two-layer model of saline wedge. II: Prediction of mean properties. *J. Hydraul. Eng.*, **113**, 1249–1263, [https://doi.org/10.1061/\(ASCE\)0733-9429\(1987\)113:10\(1249\)](https://doi.org/10.1061/(ASCE)0733-9429(1987)113:10(1249)).
- Bowden, K. F., 1965: Horizontal mixing in the sea due to a shearing current. *J. Fluid Mech.*, **21**, 83–95, <https://doi.org/10.1017/S0022112065000058>.
- Brouwer, R. L., G. P. Schramkowski, T. Verwaest, and F. Mostaert, 2015: Geïdealiseerde processtudie van systeemovergangen naar hypertroebelheid: WP 1.3 Basismodel getij en zout (in Dutch). Tech. Rep. WL2015R13\_103, Flanders Hydraulics Research, Antwerp, Belgium, 72 pp.
- Chant, R. J., C. K. Sommerfield, and S. A. Talke, 2018: Impact of channel deepening on tidal and gravitational circulation in a highly engineered estuarine basin. *Estuaries Coasts*, **41**, 1587–1600, <https://doi.org/10.1007/s12237-018-0379-6>.
- Chatwin, P. C., 1976: Some remarks and on the maintenance and of the and salinity distribution and in estuaries. *Estuarine Coastal Mar. Sci.*, **4**, 555–566, [https://doi.org/10.1016/0302-3524\(76\)90030-X](https://doi.org/10.1016/0302-3524(76)90030-X).
- De Nijs, M. A. J., J. D. Pietrzak, and J. C. Winterwerp, 2011: Advection of the salt wedge and evolution of the internal flow structure in the Rotterdam Waterway. *J. Phys. Oceanogr.*, **41**, 3–27, <https://doi.org/10.1175/2010JPO4228.1>.
- Dijkstra, Y. M., R. L. Brouwer, H. M. Schuttelaars, and G. P. Schramkowski, 2017: The iFlow modelling framework v2.4. A modular idealized process-based model for flow and transport in estuaries. *Geosci. Model Dev.*, **10**, 2691–2713, <https://doi.org/10.5194/gmd-10-2691-2017>.
- Fischer, H. B., 1972: Mass-transport mechanisms in partially stratified estuaries. *J. Fluid Mech.*, **53**, 671–687, <https://doi.org/10.1017/S0022112072000412>.
- , E. J. List, R. C. Y. Koh, and J. Imberger, 1979: *Mixing in Inland and Coastal Waters*. Academic Press, 483 pp.
- Geyer, W. R., and D. M. Farmer, 1989: Tide-induced variation of the dynamics of a salt wedge estuary. *J. Phys. Oceanogr.*, **19**, 1060–1072, [https://doi.org/10.1175/1520-0485\(1989\)019<1060:TIVOTD>2.0.CO;2](https://doi.org/10.1175/1520-0485(1989)019<1060:TIVOTD>2.0.CO;2).
- , and P. MacCready, 2014: The estuarine circulation. *Annu. Rev. Fluid Mech.*, **46**, 175–197, <https://doi.org/10.1146/annurev-fluid-010313-141302>.
- , and D. K. Ralston, 2015: Estuarine frontogenesis. *J. Phys. Oceanogr.*, **45**, 546–561, <https://doi.org/10.1175/JPO-D-14-0082.1>.
- Gong, W., and J. Shen, 2011: The response of salt intrusion to changes in river discharge and tidal mixing during the dry season in the Modaomen Estuary, China. *Cont. Shelf Res.*, **31**, 769–788, <https://doi.org/10.1016/j.csr.2011.01.011>.
- Guha, A., and G. A. Lawrence, 2013: Estuary classification revisited. *J. Phys. Oceanogr.*, **43**, 1566–1571, <https://doi.org/10.1175/JPO-D-12-0129.1>.
- Hansen, D. V., and M. Rattray, 1965: Gravitational circulation in straits and estuaries. *J. Mar. Res.*, **23**, 104–122.
- , and —, 1966: New dimensions in estuary classification. *Limnol. Oceanogr.*, **11**, 319–326, <https://doi.org/10.4319/lo.1966.11.3.0319>.
- Haralambidou, K., G. Sylaios, and V. A. Tsihrintzis, 2010: Salt-wedge propagation in a Mediterranean micro-tidal river mouth. *Estuarine Coastal Shelf Sci.*, **90**, 174–184, <https://doi.org/10.1016/j.ecss.2010.08.010>.
- Hetland, R. D., and W. R. Geyer, 2004: An idealized study of the structure of long, partially mixed estuaries. *J. Phys. Oceanogr.*, **34**, 2677–2691, <https://doi.org/10.1175/JPO2646.1>.
- Lerczak, J. A., W. R. Geyer, and R. J. Chant, 2006: Mechanisms driving the time-dependent salt flux in a partially stratified estuary. *J. Phys. Oceanogr.*, **36**, 2296–2311, <https://doi.org/10.1175/JPO2959.1>.
- , —, and D. K. Ralston, 2009: The temporal response of the length of a partially stratified estuary to changes in river flow and tidal amplitude. *J. Phys. Oceanogr.*, **39**, 915–933, <https://doi.org/10.1175/2008JPO3933.1>.
- MacCready, P., 2004: Toward a unified theory of tidally-averaged estuarine salinity structure. *Estuaries*, **27**, 561–570, <https://doi.org/10.1007/BF02907644>.
- , 2007: Estuarine adjustment. *J. Phys. Oceanogr.*, **37**, 2133–2145, <https://doi.org/10.1175/JPO3082.1>.
- , and W. R. Geyer, 2010: Advances in estuarine physics. *Annu. Rev. Mar. Sci.*, **2**, 35–58, <https://doi.org/10.1146/annurev-marine-120308-081015>.
- McKeon, M. A., A. R. Horner-Devine, and S. N. Giddings, 2020: Seasonal changes in structure and dynamics in an urbanized salt wedge estuary. *Estuaries Coasts*, <https://doi.org/10.1007/s12237-020-00788-z>.
- Monismith, S. G., W. Kimmerer, J. R. Burau, and M. T. Stacey, 2002: Structure and flow-induced and variability of the subtidal and salinity field and in and Northern San and Francisco Bay. *J. Phys. Oceanogr.*, **32**, 3003–3019, [https://doi.org/10.1175/1520-0485\(2002\)032<3003:SAFIVO>2.0.CO;2](https://doi.org/10.1175/1520-0485(2002)032<3003:SAFIVO>2.0.CO;2).
- Prandle, D., 1985: On salinity regimes and the vertical structure of residual flows in narrow tidal estuaries. *Estuarine Coastal*

- Shelf Sci.*, **20**, 615–635, [https://doi.org/10.1016/0272-7714\(85\)90111-8](https://doi.org/10.1016/0272-7714(85)90111-8).
- Pritchard, D. W., 1955: Estuarine circulation patterns. *Proc. Amer. Soc. Civ. Eng.*, **81**, 1–11.
- Ralston, D. K., W. R. Geyer, and J. A. Lerczak, 2008: Subtidal salinity and velocity in the Hudson River estuary: Observations and modelling. *J. Phys. Oceanogr.*, **38**, 753–770, <https://doi.org/10.1175/2007JPO3808.1>.
- , —, and —, 2010: Structure, variability, and salt flux in a strongly forced salt wedge estuary. *J. Geophys. Res.*, **115**, C06005, <https://doi.org/10.1029/2009JC005806>.
- Schijf, J. B., and J. C. Schönfeld, 1953: Theoretical considerations on the motion of salt and fresh water. *Proc. Minnesota Int. Hydraulic Convention*, Minneapolis, MN, ASCE and IAHR, 321–333.
- Simpson, J. H., J. Brown, J. Matthews, and G. Allen, 1990: Tidal straining, density currents, and stirring in the control of estuarine stratification. *Estuaries*, **13**, 125–132, <https://doi.org/10.2307/1351581>.
- Sorgard, E., T. Martinsen, and E. Aas, 1990: Drag coefficient at a stationary salt wedge. *J. Geophys. Res.*, **95**, 7337–7345, <https://doi.org/10.1029/JC095iC05p07337>.
- Vanlierde, E., and Coauthors, 2016: MONEOS - jaarboek monitoring WL 2015. Factual data rapportage van monitoring hydrodynamiek en fysische parameters zoals gemeten door WL in het Zeescheldebekken in 2015, Versie 3.0 (in Dutch). Tech. Rep. 12\_070, Flanders Hydraulics Research, 167 pp.
- Veldman, A. E. P., and K.-W. Lam, 2008: Symmetry-preserving upwind discretization of convection on non-uniform grids. *Appl. Numer. Math.*, **58**, 1881–1891, <https://doi.org/10.1016/j.apnum.2007.11.015>.
- Wei, X., G. P. Schramkowski, and H. M. Schuttelaars, 2016: Salt dynamics in well-mixed estuaries: Importance of advection by tides. *J. Phys. Oceanogr.*, **46**, 1457–1475, <https://doi.org/10.1175/JPO-D-15-0045.1>.
- Zimmerman, J. T. F., 1982: On the Lorentz linearization of a quadratically damped forced oscillator. *Phys. Lett.*, **89A**, 123–124, [https://doi.org/10.1016/0375-9601\(82\)90871-4](https://doi.org/10.1016/0375-9601(82)90871-4).

© Copyright [31-12-20] American Meteorological Society (AMS). For permission to reuse any portion of this work, please contact [permissions@ametsoc.org](mailto:permissions@ametsoc.org). Any use of material in this work that is determined to be “fair use” under Section 107 of the U.S. Copyright Act (17 U.S. Code §107) or that satisfies the conditions specified in Section 108 of the U.S. Copyright Act (17 USC § 108) does not require the AMS’s permission. Reproduction, systematic reproduction, posting in electronic form, such as on a website or in a searchable database, or other uses of this material, except as exempted by the above statement, requires written permission or a license from the AMS. All AMS journals and monograph publications are registered with the Copyright Clearance Center (<https://www.copyright.com>). Additional details are provided in the AMS Copyright Policy statement, available on the AMS website (<https://www.ametsoc.org/PUBSCopyrightPolicy>).